In and Out: Shuttling Atoms in Covalent Nanocrystals, from Synthesis in Molten Salts to Water-Splitting Electrocatalysis

Yang Song, Anissa Ghoridi, Fernando Igoa Saldaña, Isabel Gómez-Recio, Daniel Janisch, Edouard de Rolland Dalon, Dominique Thiaudière, Maria Luisa Ruiz-González, José González-Calbet, Benedikt Lassalle-Kaiser, et al.

Yang Song, Anissa Ghoridi, Fernando Igoa Saldaña, Isabel Gómez-Recio, Daniel Janisch, et al.. In and Out: Shuttling Atoms in Covalent Nanocrystals, from Synthesis in Molten Salts to Water-Splitting Electrocatalysis. Journal of the American Chemical Society, 2025, 147 (24), pp.20878-20887. ⟨10.1021/jacs.5c04741⟩. ⟨hal-05240391⟩

In and Out: Shuttling Atoms in Covalent Nanocrystals, from Synthesis in Molten Salts to Water-Splitting Electrocatalysis

Yang Song, Anissa Ghoridi, Fernando Igoa Saldaña, Isabel Gómez-Recio, Daniel Janisch, Edouard de Rolland Dalon, Dominique Thiaudière, Maria Luisa Ruiz-González, José M. González-Calbet, Benedikt Lassalle-Kaiser, Andrea Zitolo, Christel Laberty-Robert, and David Portehault*

ABSTRACT: Postsynthetic transformations are key to the colloidal synthesis of functional nanocrystals by offering a way to complex shapes, heterostructures, and chemical compositions. They however remain inaccessible to whole families of solids, especially those relying on covalent bonds, which crystallize at temperatures that common solvents cannot stand. Herein we show that in inorganic molten salts above 500 °C, such transformations can be triggered to deliver metallo-covalent nanocrystals previously unattainable. By incorporating silicon and phosphorus into metal nanoparticles, we synthesize nickel silicophosphide nanocrystals and demonstrate how distinct chemical bonds involving silicon or phosphorus drive their electrocatalytic properties for alkaline water oxidation and hydrogen evolution. These bonds also determine the synthesis pathway, from sequential incorporation of *p*-block elements to topotactic transformations not reported before. The ability to run such complex postsynthetic reactions of nanoparticles into molten salts paves the way to increasing complexity in compositions and chemical bonding in nanocrystals for energy conversion.

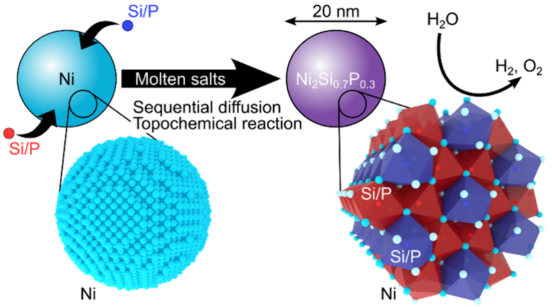

INTRODUCTION

Using nanoparticles as reagents is a way to achieve nano-objects with internal composition gradients, multiple compartments, and uncommon morphologies, leading to specific optical, transport, and catalytic properties.[1] Postsynthetic modifications have reached a high degree of sophistication for semiconductor and precious metal nanocrystals,[1−7] but they are seldom explored for other nano-objects, especially compounds combining transition metals with several *p*-block elements. Their significant covalency hinders crystallization under the usual conditions of colloidal synthesis. This has limited postsynthetic nanocrystal modifications for these materials, despite their attractive properties for semiconductors, magnetism, thermoelectricity and catalysis.[8,9]

Nickel phosphide nanocrystals are precious metal-free electrocatalysts efficient for the hydrogen evolution reaction (HER).[10] Nickel,[11,12] iron,[13] and cobalt[14] silicide nanoparticles are also precatalysts of high-performance electrocatalysts of the oxygen evolution reaction (OER). Combining phosphorus and silicon into silicophosphide nanocrystals could then deliver bifunctional HER and OER electrocatalysts from earth-abundant elements for overall water splitting. More generally, it would provide new chemical and crystallographic spaces to tune the electrocatalytic properties. From a wider perspective, metal silicophosphides remain a mostly uncharted land, despite recent works on batteries[15−23] and nonlinear optics.[24−30]

There are no metal silicophosphide nanocrystals reported yet. The incorporation of Si and P atoms into size-controlled metal nanoparticles would be an efficient way to reach such nano-objects if it could be triggered at temperatures sufficiently low to retain the particle size. With nickel as a transition metal, silicophosphides have been formed mostly from the pure elements above 800 °C.[31] Because reaction rates are enhanced in liquids, thermally stable molten salts should provide appropriate reaction media to perform silicophosphide synthesis at 400−800 °C.[11,14,32,33] This raises the question of the ability to engage metal nanoparticles into postsynthetic reactions in molten salts. Such modifications are established into common solvents,[1] but they are rare in molten salts with two recent exceptions: (i) annealing and cation exchange in iono-covalent $In_{1-x}Ga_xP$, $In_{1-x}Ga_xAs$,[34] and other III−V semiconductors[35] and (ii)

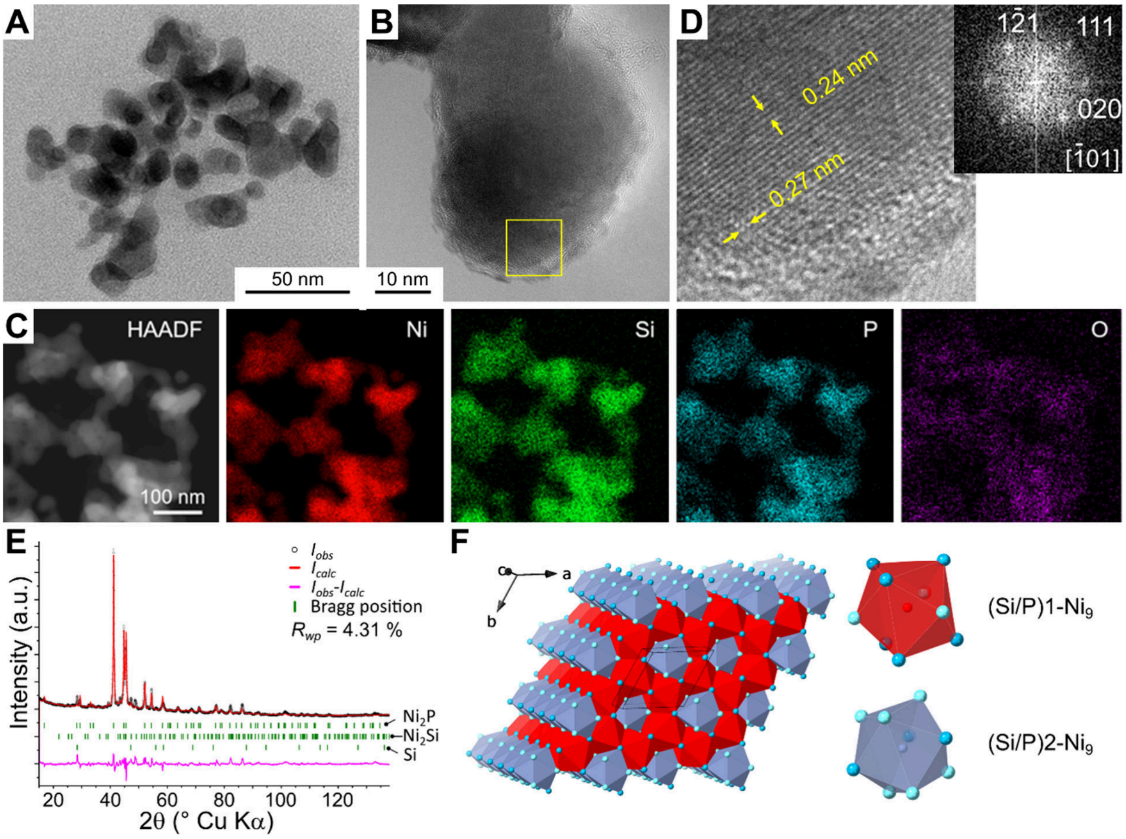

Figure 1. Morphology and crystal structure of nickel silicophosphide nanocrystals. (A, B) TEM images and (C) STEM-HAADF image and corresponding STEM-EDS chemical maps. (D) HRTEM image of the squared area in B and its corresponding FFT indexed along the *o*-Ni_2P crystal structure. (E) Powder XRD pattern and corresponding Rietveld refinement of the as-prepared ternary nanocrystals. (F) Scheme of the Ni_2P structure of the silicophosphide, where red and blue polyhedra account for the Si/P coordination spheres at the (Si/P)1 and (Si/P)2 crystallographic sites, the blue atoms showing Ni atoms. The two Ni crystallographic sites correspond to two coordination polyhedra (not shown): Ni1 coordinated to 4 P atoms and 8 Ni atoms, and Ni2 coordinated to 5 P atoms and 6 Ni atoms.

incorporation of Ni or Co atoms into silicon nanocrystals.[11,14] Inserting Si and P into nickel nanoparticles means transforming nanocrystals through the anionic component, leading to strong metallic−covalent bonding. Such reactivity is challenging in common-use solvents,[5] has never been addressed for multiple *p*-block elements, and was never explored in molten salts.

Herein, we uncover the synthesis of nickel silicophosphide nanocrystals by incorporating Si and P atoms into nickel nanoparticles in molten salts. By monitoring the reaction *in situ*, we question the order of atom incorporation in relation to the nature of chemical bonding, highlight reaction intermediates, and decipher the structural transformations that drive the formation of $Ni_2Si_{0.7}P_{0.3}$ nanocrystals and their electrocatalytic properties.

RESULTS AND DISCUSSION

Nickel Silicophosphide Nanocrystals: Synthesis, Composition, and Crystal Structure.

Nickel silicophosphide nanocrystals were prepared from Ni nanoparticles of ca. 20 nm (Figure S1), which were obtained through colloidal synthesis by reacting Ni(II) acetylacetonate, oleylamine, and trioctylphosphine (TOP).[36] The corresponding powder X-ray diffraction (XRD) pattern displays a shoulder at 46° (Cu Kα) that indicates adventitious phosphorus doping.[37] TOP is the capping ligand and is used as the phosphorus source for further transformation into a silicophosphide. The P:Ni atomic ratio is 0.15 in the initial TOP-capped nickel nanoparticle sample, according to energy-dispersive X-ray spectroscopy in a scanning electron microscope (SEM-EDS, Table S1). The Si reagent is Na_4Si_4, an efficient source of low oxidation state silicon (Figure S1).[33,38]

TOP-capped Ni nanoparticles were reacted with Na_4Si_4 in the LiI:KI eutectic salt mixture (melting point of 286 °C) at 500 °C for 4 h under argon flow. This inorganic solvent exhibits a large temperature range of stability, low vapor pressure, and inertness to reducing conditions imposed by Na_4Si_4.[33] After the reaction, the salts were washed away with methanol.

The product is made of *ca*. 20 nm nanoparticles (Figure 1A,B) that contain Ni, Si, and P homogeneously distributed according to scanning transmission electron microscopy coupled to EDS (STEM-EDS) (Figure 1C). High-resolution TEM (HRTEM)(Figure 1D) is consistent with a Ni_2P-type structure. Rietveld refinement of the powder XRD pattern (Figure 1E, Table S2) confirms crystallization in the Ni_2P structure (S. G. $P\bar{6}2m$), with lattice parameters $a = b = 6.0807$ Å and $c = 3.16159$ Å. Il'Nitskaya and Kuz'Ma showed the existence of a bulk $Ni_2P_{1-x}Si_x$ solid solution where Si substitutes for P in the Ni_2P structure.[39] *a* and *c* are significantly larger and smaller, respectively, compared to Ni_2P ($a = b = 5.8670$ Å, $c = 3.389$ Å),[40] which yields an overall increase in the unit cell volume (101.24 Å^3 compared to 101.03 Å^3), in agreement with the substitution of P by Si that exhibits a larger atomic radius. Orthorhombic Ni_2Si (*Pnma*) and diamond-like Si impurities are detected at approximately 9.5 and 0.7 wt %of the sample. The refined pattern shows peak intensities for *o*-Ni_2Si that are not fully consistent with the experimental pattern

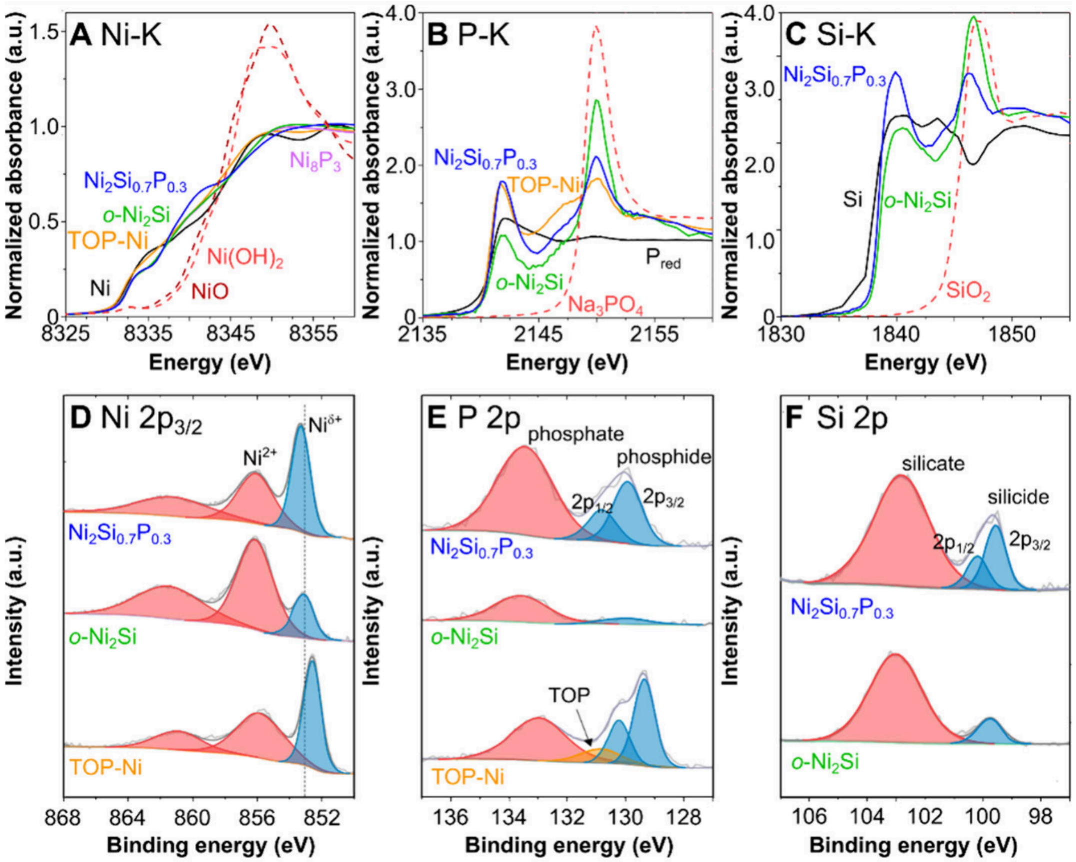

Figure 2. Electronic states in nickel silicophosphide nanocrystals. (A) Ni K-, (B) P K-, and (C) Si K-edge XANES of nickel silicophosphide nanocrystals, initial TOP-capped Ni nanoparticles (TOP-Ni), o-Ni_2Si nanocrystals, and corresponding references. In (A), the o-Ni_2Si and Ni_8P_3 curves are nearly superimposed between 8325 and 8350 eV and (D) Ni $2p_{3/2}$, (E) P 2p, and (F) Si 2p XP spectra of the silicophosphide nanocrystals, initial TOP-capped Ni nanoparticles (TOP-Ni), and o-Ni_2Si nanocrystals. In E and F, the phosphide and silicide components of o-Ni_2Si are fitted with single components because their low intensity precludes accurate fitting by considering both $2p_{1/2}$ and $2p_{3/2}$ contributions.

(e.g., at ca. 50° (2θ Cu Kα)), which could relate to additional structural defects in this byproduct. The Ni_2P structure (Figure 1F) encompasses chains of face-sharing (Si/P)Ni_9 polyhedra aligned along the c axes. Two crystallographic (Si/P) sites exist, corresponding to two types of polyhedra chains. TEM-EDS used as a local probe yields a nanocrystal composition of $Ni_{2.0\pm0.1}Si_{0.9\pm0.2}P_{0.4\pm0.1}$, which fits the expected $Ni_2Si_xP_{1-x}$ stoichiometry for a silicon-substituted Ni_2P compound. SEM-EDS (Table S1) is consistent with the $Ni_2Si_{0.7}P_{0.3}$ composition.

Following the same synthesis protocol but with lower TOP amounts on the Ni nanoparticles (P:Ni = 0.05 from SEM-EDS) yields orthorhombic o-Ni_2Si as the main product (Figure S2). $Ni_2Si_{0.7}P_{0.3}$ (Figure 1B) and o-Ni_2Si (Figure S2) exhibit layers a few nanometers thick containing O, Ni, Si, and P according to STEM-electron energy loss spectroscopy (EELS, Figure S3), which we ascribe to oxidation in contact with air.

Nickel Silicophosphide Nanocrystals: Electronic States. The Ni K-edge X-ray absorption near-edge structure (XANES) of $Ni_2Si_{0.7}P_{0.3}$ (Figure 2A, first derivative in Figure S4A) is similar to elemental nickel, initial TOP-capped nickel nanoparticles, a nickel phosphide, and o-Ni_2Si nanocrystals, thus highlighting the elemental state of Ni atoms into the silicophosphide and corresponding binary compounds. Each P K- and Si K-edge (Figure 2B,C) exhibits one contribution at low energy (2142 and 1840 eV for P and Si, respectively) and another one at higher energy (2150 and 1844 eV for P and Si, respectively). The low-energy components are ascribed to the silicophosphide with close-to-elemental states,[41] in agreement with reported values for phosphides[42] and silicides.[14] The high-energy components indicate silicates and phosphates[43] at the surface of the nanocrystals, in agreement with the O-enriched surface detected by STEM-EELS (Figure S3). The extended X-ray absorption fine structure (EXAFS, Figure S4) of the nickel silicophosphide is consistent with the crystal structure derived from XRD, with an increase in the Ni−Ni shortest distance (2.6 Å) compared to that of elemental nickel (2.5 Å) and a strong contribution of the nickel Ni−Si/P coordination at 2.2−2.4 Å. Elemental phosphorus is also detected in the precursor TOP-capped nickel nanoparticles (Figure 2B), confirming that the initial particles are P-doped. The o-Ni_2Si nanocrystals derived from TOP-poor Ni nanoparticles are also doped with phosphorus (Figure 2B), which is, however, mostly detected as phosphate species.

The Ni $2p_{2/3}$, Si 2p, and P 2p regions of X-ray photoelectron spectra (XPS, Figure 2D−F) display two contributions each. The low binding energy (BE) components show close-to-elemental Ni, Si, and P from the silicophosphide. The high BE components highlight species from surface oxidation, in agreement with STEM-EELS and XANES. The Ni $2p_{2/3}$ BE in the silicophosphide (853.3 eV) is close to the reported values for Ni_2P and the signal of o-Ni_2Si (Figure 2D),[33,42,44,45] showing a positive shift of 0.7 eV compared to elemental Ni (852.6 eV).[42,46] This indicates electron transfer from Ni to Si and P. The low BE P 2p and Si 2p silicophosphide components are

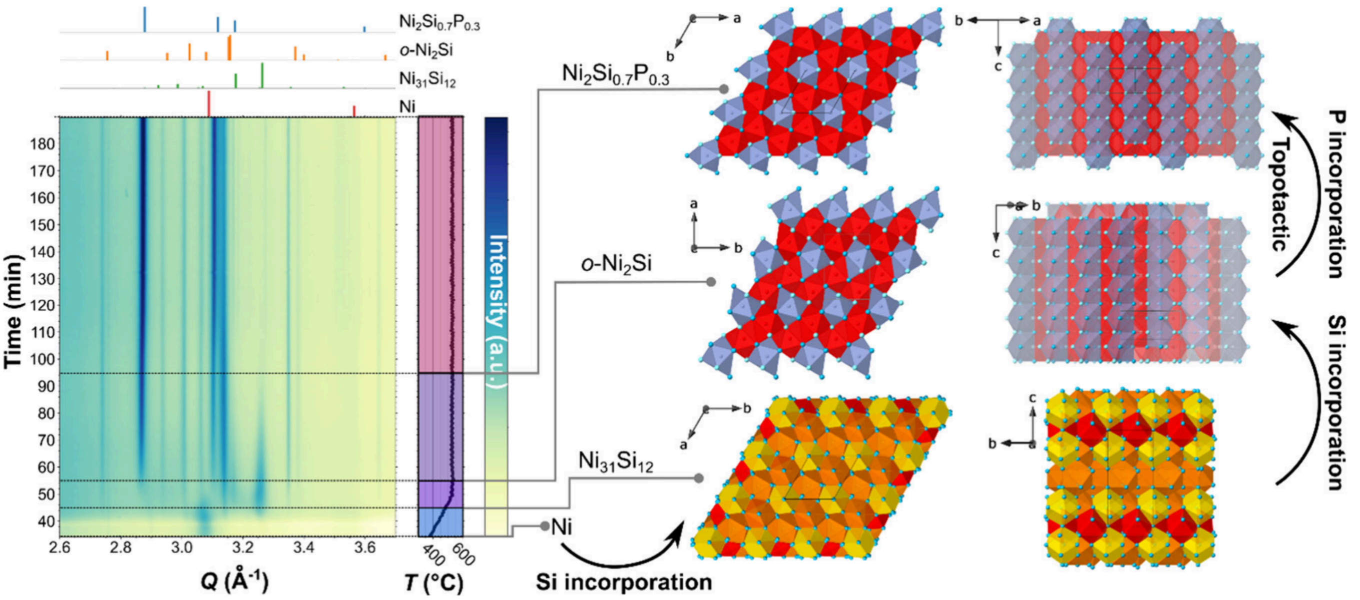

Figure 3. Reaction mechanism during the synthesis of Ni$_2$Si$_{0.7}$P$_{0.3}$ nanocrystals. *In situ* XRD diagrams recorded during heating of the reaction mixture. Some areas are highlighted in the map, showing two projections of the crystal structures for each solid-state phase detected over the course of the reaction. In the Ni$_{31}$Si$_{12}$ structure, SiNi$_9$, SiNi$_{10}$, and SiNi$_{11}$ polyhedra are shown in red, orange, and yellow, respectively. In *o*-Ni$_2$Si, all polyhedra are identical and correspond to SiNi$_9$ units. Some of these polyhedra are colorized differently to highlight the structural relationship between *o*-Ni$_2$Si and Ni$_2$Si$_{0.7}$P$_{0.3}$. In Ni$_2$Si$_{0.7}$P$_{0.3}$, (Si/P)Ni$_9$ polyhedra are colored red and blue for (Si/P)1 and (Si/P)2 crystallographic sites, respectively.

consistent with nickel phosphides[51] and *o*-Ni$_2$Si (Figure 2E,F), respectively. The P 2p contribution at 130.9 eV (Figure 2E) for the initial TOP-capped nickel nanoparticles corresponds to adsorbed trioctylphosphine.[37] These particles also contain some elemental state phosphorus, confirming the initial P-doping. The TOP component disappears in the silicophosphide, which shows full decomposition of the phosphine during the formation of the ternary nanocrystals. In agreement with XANES (Figure 2B), some phosphorus is also detected in the *o*-Ni$_2$Si nanoparticles, mostly as oxidized surface species. XANES and XPS show a higher contribution of oxidized Si species in the silicide than in the silicophosphide. This correlates with the few-nanometers-thick layer detected by TEM (Figure S2C), which we ascribe to a Si-rich oxidized layer. The higher contribution of oxidized Si species suggests that this layer is thicker on *o*-Ni$_2$Si than on Ni$_2$Si$_{0.7}$P$_{0.3}$, which then appears to be more resistant to oxidation upon air exposure.

Reaction Mechanism: Synchrotron *In Situ* X-ray Diffraction. The mechanism of transformation of the phosphine-capped nickel nanoparticles into silicophosphide nanocrystals was monitored *in situ* in the molten salts. Synchrotron *in situ* XRD was performed in transmission mode in a vertical capillary, mimicking Schlenk line conditions under argon flow. Figure 3 (see also selected 1D XRD patterns shown in Figure S7 for each temporal region of interest) shows the data recorded at one position of the capillary after melting of the eutectic mixture when heating at 10 °C min^{-1} at the temperature of synthesis (the whole experiment is displayed in Figures S5 and S6). The reaction in the laboratory is performed in alkali iodides, which are too absorbing at the incident photon energy (18 keV). The eutectic mixture LiI:KI was then replaced by the eutectic mixture LiCl:KCl melting at 353 °C. We verified that the product is similar, which validates molten chlorides as a model medium.

Before melting (Figure S5), the main diffraction peaks originate from the solvent LiCl and KCl. Ni nanoparticles are also detected. The eutectic mixture melts at 34 min when the corresponding reflections disappear, at the tabulated melting point. From then, the patterns exhibit diffuse scattering by the inorganic liquid (Figures 3 and S5). The Ni nanoparticles are the only observed crystalline species just after melting, with reflections at ~3.08 and 3.55 Å^{-1} (Figures 3 and S7). The intensity of these peaks decreases upon heating (Figures 3 and S8) until complete disappearance at 50 min, when the temperature dwell begins. Meanwhile, Ni$_{31}$Si$_{12}$, the Ni-richest silicide,[47] appears with a peak at 3.25 Å^{-1}. Ni$_{31}$Si$_{12}$ is observed over a 30 min time range and is the major phase only from ca. 45 min/454 °C to 50 min/499 °C. It rapidly evolves into *o*-Ni$_2$Si from the beginning of the 500 °C plateau. *o*-Ni$_2$Si then transforms progressively into the nickel silicophosphide (Figure 3). The crystallization sequence Ni → Ni$_{31}$Si$_{12}$ → *o*-Ni$_2$Si → Ni$_2$Si$_{0.7}$P$_{0.3}$ indicates that, although phosphorus species are at the surface of the initial Ni nanoparticles as ligands and P-doped nickel, silicon atoms arising from the decomposition of Na$_4$Si$_4$ migrate first in the core of the particles. This surprising behavior will be discussed later below in relation to the electrocatalytic properties.

The Ni → Ni$_{31}$Si$_{12}$ → *o*-Ni$_2$Si transformations occur over only a 10 min/100 °C range, which makes the *ex situ* recovery of intermediate phases challenging. *In situ* data were then necessary to monitor this evolution, especially the transient formation of Ni$_{31}$Si$_{12}$ upon thermal activation of Si diffusion in the nickel nanoparticles. The (030) reflection of Ni$_{31}$Si$_{12}$ shows peculiar behavior with a temperature increase (Figure S8): as Ni$_{31}$Si$_{12}$ appears, this peak shifts to low *Q* compared to the reference, as observed for all other phases, which is ascribed to thermal expansion. Upon further temperature increase and contrary to the expected expansion, the (030) peak moves to high *Q*, indicating a shrinkage of the *b* parameter. The Ni$_{31}$Si$_{12}$ crystal structure is made of SiNi$_9$, SiNi$_{10}$, and SiNi$_{11}$ polyhedra, while *o*-Ni$_2$Si is made only of SiNi$_9$ units. The evolution from Ni$_{31}$Si$_{12}$ to *o*-Ni$_2$Si is then accompanied by a decrease in the coordination

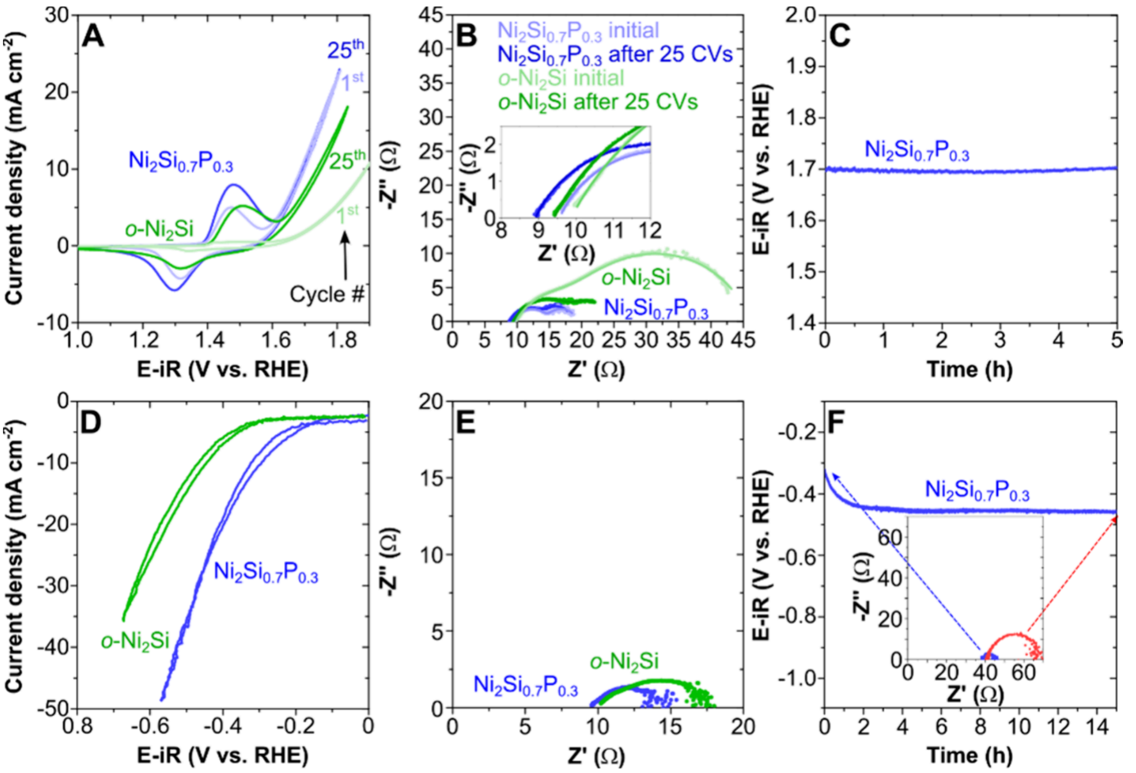

Figure 4. Alkaline water oxidation and hydrogen evolution electrocatalytic properties of $Ni_2Si_{0.7}P_{0.3}$ and *o*-Ni_2Si nanocrystals. Data were recorded in an aqueous Fe-free 0.1 M KOH electrolyte, saturated with argon and with O_2 for HER and OER, respectively. (A−C) OER properties, with (A) CV curves, (B) a Nyquist plot of EIS data recorded at 1.80 V vs RHE, and (C) CP measurement at 10 mA cm^{-2} for $Ni_2Si_{0.7}P_{0.3}$ nanocrystals after 25 CVs between 1.0 and 2.0 V vs RHE. (D−F) HER properties, with (D) CV curves at 20 mV·s^{-1}, (E) a Nyquist plot of EIS recorded at −0.60 V vs RHE, and (F) CP measurement at −10 mA cm^{-2} for $Ni_2Si_{0.7}P_{0.3}$ nanocrystals. The inset shows the EIS of the silicophosphide electrode before (blue dots) and after (red dots) CP measurement.

number of some Si atoms. This could yield a temporary shrinkage of the $Ni_{31}Si_{12}$ cell as more silicon is introduced, before transition to the *o*-Ni_2Si structure.

The intermediate *o*-Ni_2Si and the final silicophosphide $Ni_2Si_{0.7}P_{0.3}$ share the same chains of face-sharing (Si/P)Ni_9 polyhedra as the building units (Figure 3). While $Ni_2Si_{0.7}P_{0.3}$ shows two similar crystallographic (Si/P) sites, corresponding to two types of polyhedral chains, *o*-Ni_2Si exhibits only one crystallographic Si site. The transformation from *o*-Ni_2Si to $Ni_2Si_{0.7}P_{0.3}$ corresponds to a slight tilt of the chains in the (a, b) plane with a glide of these chains along the c axis by only half a polyhedron. This transformation is then topotactic: it does not request large atomic displacements or large energy input. The final structure is driven by the nature of the intermediate binary silicide and is triggered by the incorporation of phosphorus.

The diffusion of silicon and phosphorus atoms into nickel nanoparticles resembles the ability of *p*-block atoms, like silicon and boron, to diffuse outward from transition-metal silicide nanocrystals[14] and from transition-metal borosilicides[48] during water oxidation electrocatalysis. We then questioned whether the inward differentiated diffusion of *p*-block elements observed during synthesis could be reversed outward as well by an electrochemical driving force during electrocatalysis.

Alkaline Water-Splitting Electrocatalysis. The OER and HER electrocatalytic properties of the nanocrystals were investigated in a 0.1 M KOH electrolyte purified from Fe impurities.[49] The electrodes were prepared as hybrid nanocrystals/Nafion films on glassy carbon sheets without conductive additive.

Alkaline Water Oxidation and Hydrogen Evolution Electrocatalysis. The reversible anodic wave at ca. 1.5 V on the cyclic voltammograms (CVs, Figure 4A) corresponds to the Ni^{2+}/Ni^{3+} redox couple.[49] *o*-Ni_2Si undergoes activation upon cycling, when the water oxidation current increases along with the Ni redox wave area. This agrees with previous reports[11,12,33] showing that oxidized Ni is the active catalytic site for OER. $Ni_2Si_{0.7}P_{0.3}$ exhibits marginal activation, as the Ni oxidation/reduction wave area of the first CV is already as large as that for activated *o*-Ni_2Si. The catalytically active surface is therefore readily accessible for the silicophosphide, contrary to *o*-Ni_2Si that requires restructuration or dissolution of the relatively thick and passivating oxidized Si-rich layer detected by TEM (Figure S2C), XANES, and XPS. *o*-Ni_2Si and $Ni_2Si_{0.7}P_{0.3}$ nanocrystals are shown at the 25th CV overpotentials of 510 and 460 mV at 10 mA·cm^{-2}, respectively. The ternary silicophosphide is more active in OER than the binary silicide and shows an overpotential comparable to that of Ni_2P under iron-free conditions.[50,51] Electrochemical impedance spectra (EIS, Figure 4B) before the first CV and after the 25th CV (experimental details in the SI) indicate that the charge-transfer resistance only slightly evolves (Table S3) while the adsorption resistance strongly decreases only for *o*-Ni_2Si, which shows that adsorption/desorption processes of hydroxides and intermediates are more efficient on the *in situ*-generated catalytic oxyhydroxide layer.[11,12,33] The stability of the electrochemical response of $Ni_2Si_{0.7}P_{0.3}$ nanocrystals observed from CVs and by chronopotentiometry (CP, Figure 4C) over 5 h confirms that

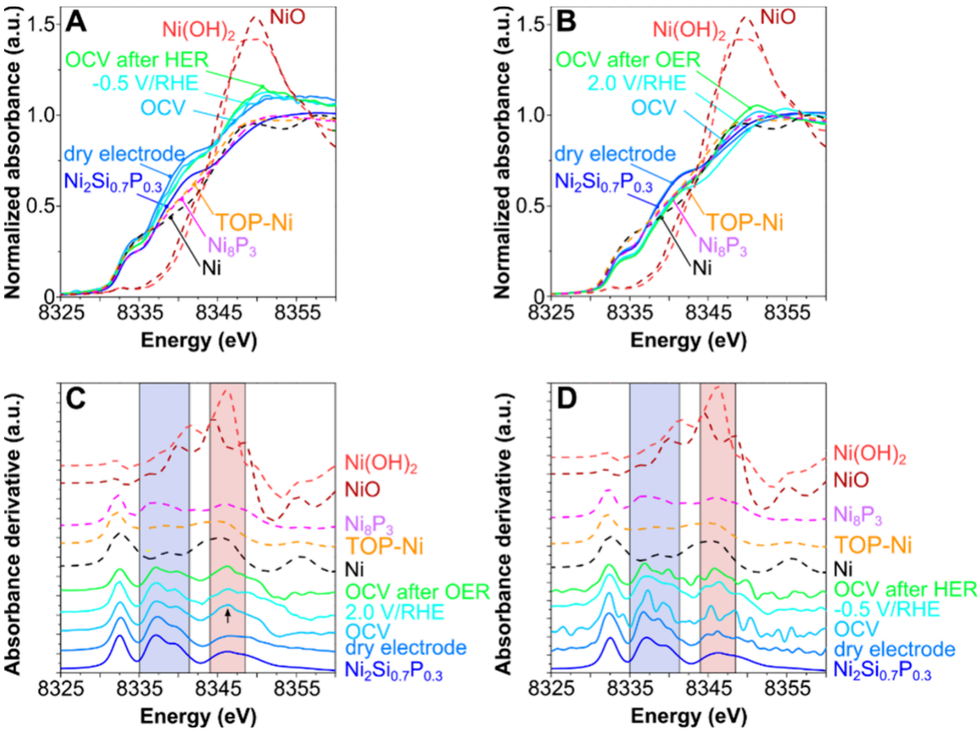

Figure 5. *In situ* XANES study of Ni$_2$Si$_{0.7}$P$_{0.3}$ and *o*-Ni$_2$Si nanocrystals during alkaline water oxidation and hydrogen evolution electrocatalysis. *In situ* (A, B) Ni K-edge XANES recorded on Ni$_2$Si$_{0.7}$P$_{0.3}$ electrodes at different stages of (A) OER and (B) HER electrocatalysis and (C, D) corresponding first derivative curves: dry electrode before use and then *in situ* XANES at the open circuit voltage (OCV) and during chronoamperometry at 2.0 V vs RHE for OER and −0.5 V vs RHE for HER. Reference spectra of the initial Ni$_2$Si$_{0.7}$P$_{0.3}$ powder, a Ni foil, P-doped nickel nanoparticles, Ni$_8$P$_3$, NiO, and Ni(OH)$_2$ are also shown for comparison. In (C), the black arrow shows a significant increase in the NiO/Ni(OH)$_2$ contribution in the oxygen-saturated electrolyte for the OER and during the corresponding OER chronoamperometry.

the surface oxidation layer is stable and accessible from the beginning of the electrochemical measurements.

CVs in an argon-saturated 0.1 M KOH electrolyte (Figure 4D) indicate that Ni$_2$Si$_{0.7}$P$_{0.3}$ is more active for HER than *o*-Ni$_2$Si, with overpotentials of 294 and 445 mV at 10 mV cm^{-2}, respectively. Ni$_2$Si$_{0.7}$P$_{0.3}$ delivers an overpotential similar to that of Ni$_2$P nanoparticles under comparable conditions.[52,53] EIS (Figure 4E) confirms that Ni$_2$Si$_{0.7}$P$_{0.3}$ is more electrically conductive than *o*-Ni$_2$Si, in agreement with a thicker native Si-rich oxide layer on *o*-Ni$_2$Si. The HER activity degrades in the first 2 h of CP (Figure 4F) due to a decrease in the electrical conductivity. This could be related to the loss of percolation in the electrode upon evacuation of H$_2$ bubbles.

Electrocatalytic Species (See Detailed Discussion in Supplementary Text 1). *In situ* XANES at the Ni K-edge (Figures 5A,C and S9) confirms that the OER activity of Ni$_2$Si$_{0.7}$P$_{0.3}$ arises from a nickel (oxyhydr)oxide layer, while the silicophosphide is maintained under HER conditions. Ni$_2$Si$_{0.7}$P$_{0.3}$ nanocrystals are more resistant to corrosion than *o*-Ni$_2$Si, which exhibits stronger structural reorganization (Figure S10). Post-catalysis Si and P K-edges XANES (Figure S11), STEM-HAADF and STEM-EDS (Figure 6) show that the crystalline Ni$_2$P-like structure is maintained, with Ni, Si, and P remaining in the core. SEM-EDS (Table S4) indicates leaching of Si during the OER, while the P content does not evolve significantly. TEM (Figure 6) highlights an amorphous oxide layer on the nanocrystal surface that is thicker than on pristine nanocrystals (∼10 vs 3 nm, Figure 1A) and contains only oxidized Ni and Si according to XPS (Figure S12). This layer may form during the recovery of the electrode after operation under HER reductive conditions. The silicophosphide nanocrystals mostly retain their structure during electrocatalysis. A disordered (oxyhydr)oxide layer forms at their surface, especially under OER conditions, like on previously reported silicides and borosilicides,[14,48] but the silicophosphide exhibits unusual behavior, as the partitioning of the different *p*-block elements between the metallic core and the oxidic surface layer is differentiated.

Diffusion of *p*-Block Elements during Synthesis and Electrocatalysis. During alkaline water oxidation electrocatalysis, silicon diffuses outward from Ni$_2$Si$_{0.7}$P$_{0.3}$ nanocrystals (Figure 7) while phosphorus remains mostly in the core, which maintains a silicophosphide composition and structure. This mobility, which is higher for silicon than for phosphorus, is similar to what we observed during synthesis, where silicon diffuses first into the metal nanoparticles (Figure 7). These differences in atomic diffusion relate to the nature of bonding. P is indeed more electronegative than Ni ($\chi_P = 2.2 > \chi_{Ni} = 1.9$), while Si and Ni have very close and low electronegativity values ($\chi_{Si} = 1.9$). Therefore, bonding in nickel phosphides is more iono-covalent than in nickel silicides, which exhibit a stronger metallic character. On the synthesis heating ramp, less directional and less localized Ni−Si bonds facilitate Si diffusion and fast restructuration into metal silicides, while phosphorus is restricted to the surface. This is supported by the diffusion coefficient of Si in nickel at the synthesis temperature (530 °C) of ca. 10^{-20} m^2·s^{-1}, 2 orders of magnitude higher than for P in P-doped nickel.[54,55] The corresponding diffusion lengths over 30 min are 4 and 0.4 nm, respectively. The former value is commensurate with the radii of the Ni nanoparticles and supports their rapid conversion to silicides before phosphorus can diffuse.

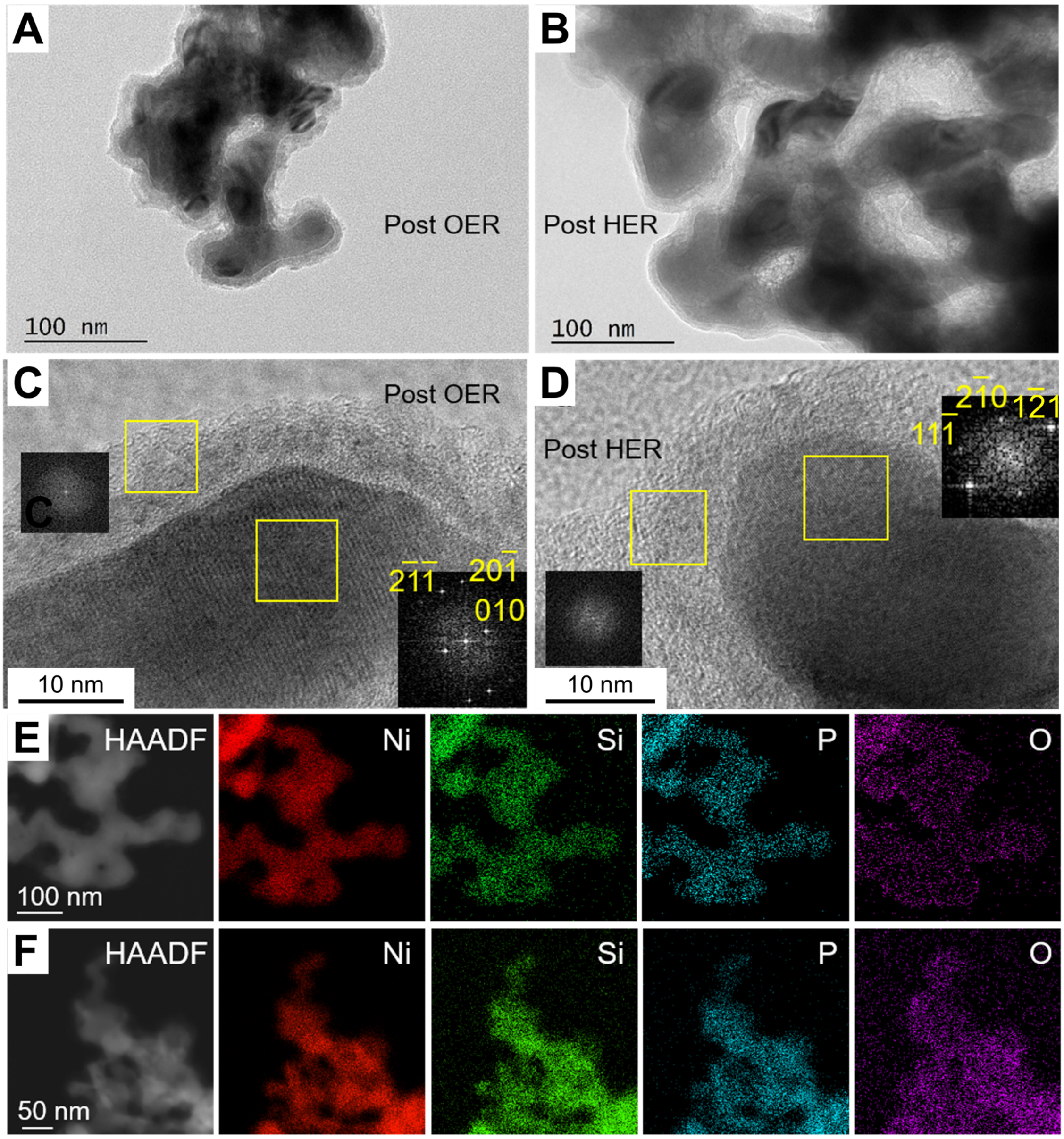

Figure 6. Post-catalysis $Ni_2Si_{0.7}P_{0.3}$ nanocrystals. TEM images after (A) 5 h OER at 2.0 V vs RHE and (B) 15 h HER at −0.5 V vs RHE. (C, D) Corresponding HRTEM images, with FFTs of the yellow squared areas. STEM-HAADF images and STEM-EDS chemical maps after (E) 5 h of OER and (F) 15 h of HER. In (C) and (D), the lattice fringes are indexed along the $Ni_2Si_{0.7}P_{0.3}$ structure, in agreement with XRD.

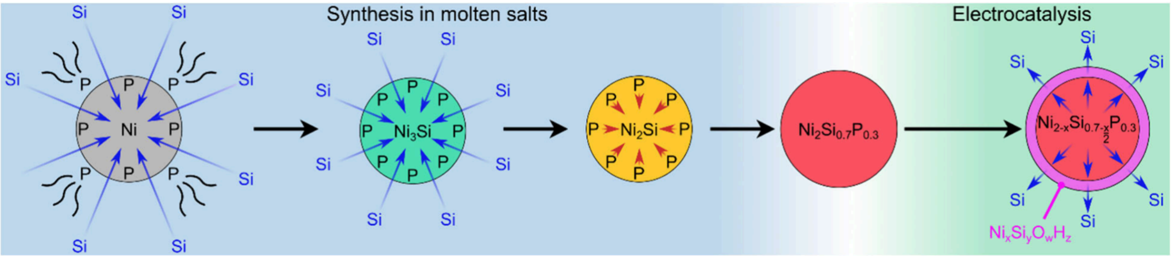

Figure 7. Transformations of nickel, nickel silicide, and nickel silicophosphide nanocrystals. Differentiated diffusion of silicon and phosphorus atoms into nickel-based nanocrystals occurs during synthesis in molten salts but also during electrocatalysis.

■ CONCLUSIONS

Our results demonstrate that the incorporation of two *p*-block elements, Si and P, into metal nanoparticles occurs through a complex sequence activated when the particles are dispersed into molten salts. These high-temperature inorganic solvents are essential for reacting dispersed nanocrystals toward the formation of metallo-covalent silicophosphides, as covalent bonds between the *p*-block elements and metal atoms impose significant energy input for crystallization.

The conversion of the initial metal nanoparticles proceeds by the sequential diffusion of silicon and phosphorus atoms, as also observed in the reactivity of the silicophosphide nanocrystals during alkaline water splitting electrocatalysis: Si is more prone to diffuse in and out of the nanocrystals than is phosphorus. The nature of the chemical bonds engaging *p*-block atoms dictates this behavior, as Si with its metallic−covalent bonding to Ni diffuses into the metal nanoparticles faster than P involved in iono-covalent bonds. The crystallization pathway we uncover is unique for transformations of nano-objects, comprising not only sequential atomic diffusion but also topotactic modifications of the crystal structures, with small collective atom movements. This opens new tracks in the search for nanocrystals based on metal *p*-block element compounds, as the metallicity−covalency cursor appears to be a guideline to control atom diffusion, hence the nature of reaction intermediates and their transformations. This also affects the corrosion resistance and partitioning of elements between catalytic layers and electrically conductive cores. This provides new guidelines to design original nano-objects for electrocatalysis.

EXPERIMENTAL METHODS

Reagents. Lithium iodide (99%, Alfa Aesar), potassium iodide (99%, Sigma-Aldrich), silicon nanoparticles (99%, Nanomakers), sodium hydride (95%, Sigma-Aldrich), nickel(II) acetylacetonate (95%, Ni(acac)$_2$, Strem Chemicals), and trioctylphosphine (TOP, 97%, P(C$_8$H$_{16}$)$_3$, Strem Chemicals) were stored and manipulated as received in an Ar-filled glovebox ($H_2O < 0.5$ ppm, $O_2 < 0.5$ ppm). Oleylamine (technical grade 70%, Sigma-Aldrich) was stored and used in air. Acetone (VWR Normapur grade), tetrahydrofuran (THF, VWR Normapur grade), and methanol (VWR Normapur grade) were used for washing.

Synthesis of Ni Nanoparticles. The synthesis is based on a protocol reported elsewhere.[35] 20.8 g (25.6 mL, 78 mmol) of oleylamine and a Teflon-coated stir bar were put in a 50 mL three-necked round-bottomed flask connected to a reflux condenser and a Schlenk line. Then, oleylamine was stirred and degassed at room temperature under vacuum during 30 min to remove dissolved air. Afterward, 2 g (7.8 mmol) of Ni(acac)$_2$ and 2.1 mL (4.7 mmol) of TOP were added. With a heating mantle, the mixture was degassed at 100 °C for 3 min to remove the side products. Then, the contents were rapidly heated to 220 °C and maintained for 2 h under a nitrogen flow. The suspension was cooled to room temperature and transferred to a centrifuge tube for washing. The nanoparticles were isolated by centrifugation at 21000 rpm for 3 min. After the supernatant was removed, 30 mL of acetone and 10 mL of THF were added. Then, this process was repeated nine times. The washed nanoparticles were dried in a Schlenk tube under vacuum and then stored in an Ar-filled glovebox for further manipulation.

Synthesis of Na_4Si_4. This synthesis is an improvement of a reported protocol.[10] 470 mg (20 mmol) of NaH and 500 mg (20 mmol) of Si nanoparticles were ball-milled for 2 min at 20 Hz. Then, the fine mixture was loaded into a pyrolytic *h*-BN crucible (cylinder Ø25 × H60 mm) covered with a cap of the same material and then placed in a bottom-closed quartz tube. The tube was heated in a vertical furnace at 395 °C for 48 h under Ar flow. After cooling, the system was transferred to an Ar-filled glovebox. The as-synthesized sample was a dark pellet with another white pellet on top. The latter, corresponding to Na_2O and NaOH, was scratched away. The obtained Na_4Si_4 powder was stored in the Ar-filled glovebox until it reacted with Ni nanoparticles.

***Caution!* Na_4Si_4 powder is air-sensitive and burns spontaneously when exposed to water.** All manipulations were performed by handling these powders under an inert atmosphere, except when stated otherwise.

Synthesis of Ternary Nickel Silicophosphide Nanoparticles. An 88 mg (1.5 mmol) sample of Ni nanoparticles, 45 mg (0.21 mmol) of Na_4Si_4, 2.9 g of LiI (21.7 mmol), and 2.1 g of KI (12.7 mmol) were ball-milled for 2 min at 20 Hz to get a homogeneous mixture, which was later transferred to a glassy carbon crucible (Ø10 × H200 mm). The crucible was placed in a bottom-closed quartz tube and then connected to a Schlenk line under Ar flow. A vertical furnace from Eraly was preheated to the reaction temperature of 500 °C. Then, the quartz tube was put in the furnace. After the temperature was held for 4 h under Ar flow, the hot quartz tube was taken out and cooled down. The as-prepared mixture was washed in methanol by seven cycles of centrifugation/redispersion and was later dried in a Schlenk tube under vacuum overnight. The dried powder was transferred and stored in an Ar-filled glovebox.

Supporting Information

Details of characterization methods, Figures S1−S13, Tables S1−S4, and supplementary text 1 on *in situ* and post-catalysis studies of electrocatalysis (PDF)

AUTHOR INFORMATION

Corresponding Author

David Portehault − *Sorbonne Université, CNRS, Laboratoire de Chimie de la Matière Condensée de Paris (CMCP), F-75005 Paris, France;* orcid.org/0000-0003-4914-4913; Email: david.portehault@sorbonne-universite.fr

Authors

Yang Song − *Sorbonne Université, CNRS, Laboratoire de Chimie de la Matière Condensée de Paris (CMCP), F-75005 Paris, France*

Anissa Ghoridi − *Sorbonne Université, CNRS, Laboratoire de Chimie de la Matière Condensée de Paris (CMCP), F-75005 Paris, France*

Fernando Igoa Saldaña − *Sorbonne Université, CNRS, Laboratoire de Chimie de la Matière Condensée de Paris (CMCP), F-75005 Paris, France*

Isabel Gómez-Recio − *Sorbonne Université, CNRS, Laboratoire de Chimie de la Matière Condensée de Paris (CMCP), F-75005 Paris, France,* orcid.org/0000-0001-7788-9037

Daniel Janisch − *Sorbonne Université, CNRS, Laboratoire de Chimie de la Matière Condensée de Paris (CMCP), F-75005 Paris, France*

Edouard de Rolland Dalon − *Sorbonne Université, CNRS, Laboratoire de Chimie de la Matière Condensée de Paris (CMCP), F-75005 Paris, France*

Dominique Thiaudière − *Synchrotron SOLEIL, L'Orme des Merisiers, 91190 Saint-Aubin, France*

Maria Luisa Ruiz-González − *Dpto. de Química Inorgánica I, Facultad de Ciencias Químicas, Universidad Complutense, 28040 Madrid, Spain*

José M. González-Calbet − *Dpto. de Química Inorgánica I, Facultad de Ciencias Químicas, Universidad Complutense, 28040 Madrid, Spain;* orcid.org/0000-0002-6481-6506

Benedikt Lassalle-Kaiser − *Synchrotron SOLEIL, L'Orme des Merisiers, 91190 Saint-Aubin, France;* Present Address: ITODYS, CNRS, UMR086, Université Paris Cité, 15 rue Jean-Antoine de Baïf, 75013 Paris, France*;* orcid.org/0000-0003-2141-2496

Andrea Zitolo − *Synchrotron SOLEIL, L'Orme des Merisiers, 91190 Saint-Aubin, France;* orcid.org/0000-0002-2187-6699

Christel Laberty-Robert − *Sorbonne Université, CNRS, Laboratoire de Chimie de la Matière Condensée de Paris (CMCP), F-75005 Paris, France;* orcid.org/0000-0003-3230-3164

ACKNOWLEDGMENTS

This project has received funding from the European Research Council (ERC) Consolidator Grant GENESIS under the European Union's Horizon 2020 research and innovation programme (grant agreement no. 864850). Y.S. thanks the China Science Council for funding. The X-ray absorption spectroscopy experiments at the SAMBA and LUCIA beamlines at Synchrotron SOLEIL have been funded by SOLEIL as user proposal 20210428. *In situ* XRD experiments at DIFFABS beamline of SOLEIL were supported under the user proposal 20210456. The authors acknowledge the support by the Spanish Ministry of Science and Innovation through Research Project PID2020-113753RB-I00 and the Spanish National Centre for Electron Microscopy (ELECMI National Singular Scientific Facility) for the provision of corrected aberration microscopy. F.I.S. acknowledges the French Ministry for Research and the Doctoral School ED397 for funding.

REFERENCES

(1) Manna, L.; Cheon, J.; Schaak, R. E. Why Do We Care about Studying Transformations in Inorganic Nanocrystals? *Acc. Chem. Res.* **2021**, *54* (7), 1543−1544.

(2) Schaak, R. E.; Steimle, B. C.; Fenton, J. L. Made-to-Order Heterostructured Nanoparticle Libraries. *Acc. Chem. Res.* **2020**, *53* (11), 2558−2568.

(3) Toso, S.; Baranov, D.; Manna, L. Metamorphoses of Cesium Lead Halide Nanocrystals. *Acc. Chem. Res.* **2021**, *54* (3), 498−508.

(4) Han, H.; Yao, Y.; Robinson, R. D. Interplay between Chemical Transformations and Atomic Structure in Nanocrystals and Nano-clusters. *Acc. Chem. Res.* **2021**, *54* (3), 509−519.

(5) Saruyama, M.; Sato, R.; Teranishi, T. Transformations of Ionic Nanocrystals via Full and Partial Ion Exchange Reactions. *Acc. Chem. Res.* **2021**, *54* (4), 765−775.

(6) Lim, Y.; Han, J. H.; Cheon, J. Chemical Transformations of Anisotropic Platelets and Spherical Nanocrystals. *Acc. Chem. Res.* **2021**, *54* (7), 1565−1574.

(7) Veglak, J. M.; Tsai, A.; Soliman, S. S.; Dey, G. R.; Schaak, R. E. Disentangling Competitive and Synergistic Chemical Reactivities During the Seeded Growth of High-Entropy Alloys on High-Entropy Metal Sulfide Nanoparticles. *J. Am. Chem. Soc.* **2024**, *146* (28), 19521 − 19536.

(8) Carenco, S.; Portehault, D.; Boissière, C.; Mézailles, N.; Sanchez, C. Nanoscaled Metal Borides and Phosphides: Recent Developments and Perspectives. *Chem. Rev.* **2013**, *113*(10), 7981−8065 .

(9) Chen, X.; Liang, C. Transition Metal Silicides: Fundamentals, Preparation and Catalytic Applications. *Catal. Sci. Technol.* **2019**, *9* (18), 4785−4820.

(10) Callejas, J. F.; Read, C. G.; Roske, C. W.; Lewis, N. S.; Schaak, R. CI. Synthesis, Characterization, and Properties of Metal Phosphide Catalysts for the Hydrogen-Evolution Reaction. *Chem. Mater.* **2016**, *28* (17), 6017−6044.

(11) Song, Y.; Casale, S.; Miche, A.; Montero, D.; Laberty-Robert, C.; Portehault, D. Converting Silicon Nanoparticles into Nickel Iron Silicide Nanocrystals within Molten Salts for Water Oxidation Electrocatalysis. *J. Mater. Chem. A* **2022**, *10* (3), 1350−1358.

(12) Mondal, I.; Hausmann, J. N.; Vijaykumar, G.; Mebs, S.; Dau, H.; Driess, M.; Menezes, P. W. Nanostructured Intermetallic Nickel Silicide (Pre)Catalyst for Anodic Oxygen Evolution Reaction and Selective Dehydrogenation of Primary Amines. *Adv. Energy Mater.* **2022**, *12* (25), No. 2200269.

(13) Hausmann, J. N.; Beltran-Suito, R.; Mebs, S.; Hlukhyy, V.; Fassler, T. F.; Dau, H.; Driess, M.; Menezes, P. W. Evolving Highly Active Oxidic Iron(III) Phase from Corrosion of Intermetallic Iron Silicide to Master Efficient Electrocatalytic Water Oxidation and Selective Oxygenation of 5-Hydroxymethylfurfural. *Adv. Mater.* **2021**, *33* (27), No. 2008823.

(14) Song, Y.; Gómez-Recio, I.; Ghoridi, A.; Igoa Saldaña, F.; Janisch, D.; Sassoye, C.; Dupuis, V.; Hrabovsky, D.; Ruiz-González, M. L.; González-Calbet, J. M.; Casale, S.; Zitolo, A.; Lassalle-Kaiser, B.; Laberty-Robert, C.; Portehault, D. Heterostructured Cobalt Silicide Nanocrystals: Synthesis in Molten Salts, Ferromagnetism, and Electrocatalysis. *J. Am. Chem. Soc.* **2023**, *145* (35), 19207−19217.

(15) Coquil, G.; Fullenwarth, J.; Grinbom, G.; Sougrati, M. T.; Stievano, L.; Zitoun, D.; Monconduit, L. FeSi$_{4P}$4: A Novel Negative Electrode with Atypical Electrochemical Mechanism for Li and Na-Ion Batteries. *J. Power Sources* **2017**, *372*, 196−203.

(16) Liu, Q.; Wang, J.; Luo, Y.; Miao, L.; Yan, Y.; Xue, L.; Zhang, W. Facile Synthesis of $FeSi_4P_4$ and Its Sodium Ion Storage Performance. *Electrochim. Acta* **2017**, *247*, 820−825.

(17) Li, W.; Li, X.; Liao, J.; Zhao, B.; Zhang, L.; Huang, L.; Liu, G.; Guo, Z.; Liu, M. A New Family of Cation-Disordered Zn(Cu)−Si−P Compounds as High-Performance Anodes for next-Generation Li-Ion Batteries. *Energy Environ. Sci.* **2019**, *12* (7), 2286−2297.

(18) Li, W.; Liao, J.; Li, X.; Zhang, L.; Zhao, B.; Chen, Y.; Zhou, Y.; Guo, Z.; Liu, M. $Zn(Cu)Si_{2+x}P_3$ Solid Solution Anodes for High-Performance Li-Ion Batteries with Tunable Working Potentials. *Adv. Funct. Mater.* **2019**, *29* (34), No. 1903638.

(19) Zhang, X.; Li, W.; Chen, H. High-Capacity $CuSi_2P_3$ -Based Semisolid Anolyte for Redox Flow Batteries. *ACS Appl. Mater. Interfaces* **2021**, *13* (34), 40552−40561.

(20) Nazarian-Samani, M.; Nazarian-Samani, M.; Haghighat-Shishavan, S.; Kim, K.-B. Si,P Vacancy-Enriched CoSi3P3 Anode with Exceptional Li Storage Performance. *Energy Storage Mater.* **2021**, *36*, 229−241.

(21) Li, W.; Ma, Q.; Shen, P.; Zhou, Y.; Soule, L.; Li, Y.; Wu, Y.; Zhang, H.; Liu, M. Yolk-Shell Structured $CuSi_2P_3$@Graphene Nano-composite Anode for Long-Life and High-Rate Lithium-Ion Batteries. *Nano Energy* **2021**, *80*, No. 105506.

(22) Nazarian-Samani, M.; Nazarian-Samani, M.; Haghighat-Shishavan, S.; Kim, K.-B. Efficient Stress Alleviation and Interface Regulation in Cu_4SiP_8-CNT Hybrid for Ultra-Durable Li and Na Storage. *Nano Energy* **2021**, *86*, No. 106134.

(23) Nazarian-Samani, M.; Nazarian-Samani, M.; Haghighat-Shishavan, S.; Kim, K.-B. Fe^{3+}-Derived Boosted Charge Transfer in an $FeSi_4P_4$ Anode for Ultradurable Li-Ion Batteries. *ACS Nano* **2022**, *16* (8), 12606−12619.

(24) Mark, J.; Wang, J.; Wu, K.; Lo, J. G.; Lee, S.; Kovnir, K. $Ba_2Si_3P_6$: 1D Nonlinear Optical Material with Thermal Barrier Chains. *J. Am. Chem. Soc.* **2019**, *141* (30), 11976−11983.

(25) Yu, T.; Wang, S.; Zhang, X.; Li, C.; Qiao, J.; Jia, N.; Han, B.; Xia, S.-Q.; Tao, X. $MnSiP_2$: A New Mid-IR Ternary Phosphide with Strong SHG Effect and Ultrabroad Transparency Range. *Chem. Mater.* **2019**, *31* (6), 2010−2018.

(26) Lee, S.; Carnahan, S. L.; Akopov, G.; Yox, P.; Wang, L.; Rossini, A. J.; Wu, K.; Kovnir, K. Noncentrosymmetric Tetrel Pnictides $RuSi_4P_4$ and $IrSi_3P_3$: Nonlinear Optical Materials with Outstanding Laser Damage Threshold. *Adv. Funct. Mater.* **2021**, *31* (16), No. 2010293.

(27) Chen, J.; Chen, H.; Xu, F.; Cao, L.; Jiang, X.; Yang, S.; Sun, Y.; Zhao, X.; Lin, C.; Ye, N. $Mg_2In_3Si_2P_7$: A Quaternary Diamond-like

Phosphide Infrared Nonlinear Optical Material Derived from $ZnGeP_2$. *J. Am. Chem. Soc.* **2021**, *143* (27), 10309−10316.

(28) Yox, P.; Porter, A. P.; Dorn, R. W.; Kyveryga, V.; Rossini, A. J.; Kovnir, K. Semiconducting Silicon−Phosphorus Frameworks for Caging Exotic Polycations. *Chem. Commun.* **2022**, *58* (55), 7622−7625.

(29) Zhao, X.; Lin, C.; Chen, J.; Xu, F.; Yang, S.; Peng, G.; Tian, H.; Han, Y.; Li, B.; Luo, M.; Ye, N. $BaSi_7P_{10}$ and $SrSi_7P_{10}$: Two Infrared Nonlinear Optical Phosphides with T2 Supertetrahedra Exhibiting Strong Second-Harmonic Generation Effects. *Adv. Opt. Mater.* **2022**, *10* (16), No. 2200045.

(30) Song, Y.; Lin, C.; Wang, C.; Zhou, Y.; Fang, S.; Dong, P.; Li, B.; Ye, N.; Zhao, X.; Luo, M. $EuSi_7P_{10}$: An Inorganic Supramolecular Nonlinear Optical Crystal Exhibiting Strong Second-Harmonic Generation Response. *Inorg. Chem.* **2024**, *63* (24), 10932−10937.

(31) Liu, Y.; Cao, D.; Tu, H.; Su, X.; Wang, J.; Wu, C.; Peng, H. Phase Equilibria of the Ni−Si−P System at 800 °C. *J. Alloys Compd.* **2013**, *577*, 643−649.

(32) Portehault, D.; Delacroix, S.; Gouget, G.; Grosjean, R.; Chan-Chang, T.-H.-C. Beyond the Compositional Threshold of Nanoparticle-Based Materials. *Acc. Chem. Res.* **2018**, *51* (4), 930−939.

(33) Kumar, R.; Bahri, M.; Song, Y.; Gonell, F.; Thomas, C.; Ersen, O.; Sanchez, C.; Laberty-Robert, C.; Portehault, D. Phase Selective Synthesis of Nickel Silicide Nanocrystals in Molten Salts for Electrocatalysis of the Oxygen Evolution Reaction. *Nanoscale* **2020**, *12* (28), 15209−15213.

(34) Srivastava, V.; Kamysbayev, V.; Hong, L.; Dunietz, E.; Klie, R. F.; Talapin, D. V. Colloidal Chemistry in Molten Salts: Synthesis of Luminescent $In_{1-x}Ga_xP$ and $In_{1-x}Ga_xAs$ Quantum Dots. *J. Am. Chem. Soc.* **2018**, *140* (38), 12144−12151.

(35) Srivastava, V.; Liu, W.; Janke, E. M.; Kamysbayev, V.; Filatov, A. S.; Sun, C. J.; Lee, B.; Rajh, T.; Schaller, R. D.; Talapin, D. V. Understanding and Curing Structural Defects in Colloidal GaAs Nanocrystals. *Nano Lett.* **2017**, *17* (3), 2094−2101.

(36) Carenco, S.; Boissière, C.; Nicole, L.; Sanchez, C.; Le Floch, P.; Mézailles, N. Controlled Design of Size-Tunable Monodisperse Nickel Nanoparticles. *Chem. Mater.* **2010**, *22* (4), 1340−1349.

(37) Carenco, S.; Liu, Z.; Salmeron, M. The Birth of Nickel Phosphide Catalysts: Monitoring Phosphorus Insertion into Nickel. *ChemCatCh-em.* **2017**, *9* (12), 2318−2323.

(38) Song, Y.; Gómez-Recio, I.; Kumar, R.; Diogo, C. C.; Casale, S.; Génois, I.; Portehault, D. A Straightforward Approach to High Purity Sodium Silicide Na_4Si_4. *Dalton Trans.* **2021**, *50* (45), 16703−16710.

(39) Il'Nitskaya, O. N.; Kuz'Ma, Y. B. The Reaction of Nickel with Silicon and Phosphorus. *React. Nickel Silicon Phosphorus* **1992**, *37* (4), 364−366.

(40) Fruchart, R.; Roger, A.; Senateur, J. P. Crystallographic and Magnetic Properties of Solid Solutions of the Phosphides M_2P, M = Cr, Mn, Fe, Co, and Ni. *J. Appl. Phys.* **1969**, *40* (3), 1250.

(41) Naftel, S. J.; Coulthard, I.; Sham, T. K.; Das, S. R.; Xu, D.-X. Structural and Electronic Property Evolution of Nickel and Nickel Silicide Thin Films on Si(100) from Multicore X-Ray-Absorption Fine-Structure Studies. *Phys. Rev. B* **1998**, *57* (15), 9179−9185.

(42) Blanchard, P. E. R.; Grosvenor, A. P.; Cavell, R. G.; Mar, A. X-Ray Photoelectron and Absorption Spectroscopy of Metal-Rich Phosphides M2P and M3P (M = Cr-Ni). *Chem. Mater.* **2008**, *20* (22), 7081−7088.

(43) Flank, A. M.; Karnatak, R. C.; Blancard, C.; Esteva, J. M.; Lagarde, P.; Connerade, J. P. Probing Matrix Isolated SiO Molecular Clusters by X-Ray Absorption Spectroscopy. *Z. Für Phys. At. Mol. Clust.* **1991**, *21* (4), 357−366.

(44) Cao, Y.; Nyborg, L.; Jelvestam, U. XPS Calibration Study of Thin-film Nickel Silicides. *Surf. Interface Anal.* **2009**, *41* (6), 471−483.

(45) Zhang, Y.; Liu, Y.; Ma, M.; Ren, X.; Liu, Z.; Du, G.; Asiri, A. M.; Sun, X. A Mn-Doped Ni_2P Nanosheet Array: An Efficient and Durable Hydrogen Evolution Reaction Electrocatalyst in Alkaline Media. *Chem. Commun.* **2017**, *53* (80), 11048−11051.

(46) Masa, J.; Piontek, S.; Wilde, P.; Antoni, H.; Eckhard, T.; Chen, Y.; Muhler, M.; Apfel, U.; Schuhmann, W. Ni-Metalloid (B, Si, P, As, and Te) Alloys as Water Oxidation Electrocatalysts. *Adv. Energy Mater.* **2019**, *9*, No. 1900796.

(47) Zhang, P.; Ji, S. J.; Zhang, D.; Xue, H. G.; Suen, N. T. Synthesis, Crystal Structure, Electronic Structure, and Electrocatalytic Hydrogen Evolution Reaction of Synthetic Perryite Mineral. *Inorg. Chem.* **2021**, *60* (5), 3006−3014.

(48) Janisch, D.; Igoa Saldaña, F.; De Rolland Dalon, E.; Inocêncio, VC. M.; Song, Y.; Autran, P.-O.; Miche, A.; Casale, S.; Portehault, D. Covalent Transition Metal Borosilicides: Reaction Pathways in Molten Salts for Water Oxidation Electrocatalysis. *J. Am. Chem. Soc.* **2024**, *146* (31), 21824−21836.

(49) Trotochaud, L.; Young, S. L.; Ranney, J. K.; Boettcher, S. W. Nickel−Iron Oxyhydroxide Oxygen-Evolution Electrocatalysts: The Role of Intentional and Incidental Iron Incorporation. *J. Am. Chem. Soc.* **2014**, *136* (18), 6744−6753.

(50) Stern, L. A.; Feng, L.; Song, F.; Hu, X. Ni_2P as a Janus Catalyst for Water Splitting: The Oxygen Evolution Activity of Ni_2P Nanoparticles. *Energy Environ. Sci.* **2015**, *8* (8), 2347−2351.

(51) Valizadeh, A.; Najafpour, M. M. Is Nickel Phosphide an Efficient Catalyst for the Oxygen-Evolution Reaction at Low Overpotentials?*New J. Chem.* **2020**, *44* (45), 19630−19641.

(52) Popcz un,E. J.; McKone, J. R.; Read, C. G.; Biacchi, A. J.; Wiltrout, A. M.; Lewis, N. S.; Schaak, R. E. Nanostructured Nickel Phosphide as an Electrocatalyst for the Hydrogen Evolution Reaction. *J. Am. Chem. Soc.* **2013**, *135* (25), 9267−9270.

(53) Hu, C.; Lv, C.; Liu, S.; Shi, Y.; Song, J.; Zhang, Z.; Cai, J.; Watanabe, A. Nickel Phosphide Electrocatalysts for Hydrogen Evolution Reaction. *Catalysts* **2020**, *10* (2), 188.

(54) Garnier, T.; Manga, V. R.; Bellon, P.; Trinkle, D. R. Diffusion of Si Impurities in Ni under Stress: A First-Principles Study. *Phys. Rev. B* **2014**, *90* (2), No. 024306.

(55) Ke, J.-H.; Young, G. A.; Tucker, J. D. Ab Initio Study of Phosphorus Effect on Vacancy-Mediated Process in Nickel Alloys − An Insight into Ni_2Cr Ordering. *Acta Mater.* **2019**, *172*, 30−43.

Supporting information

In and out: shuttling atoms in covalent nanocrystals, from synthesis in molten salts to water splitting electrocatalysis

Yang Song,[a] Anissa Ghoridi,[a] Fernando Igoa Saldaña,[a] Isabel Gómez-Recio,[a] Daniel Janisch,[a] Edouard de Rolland Dalon,[a] Dominique Thiaudière,[b] Maria Luisa Ruiz-González,[c] José M. González-Calbet,[c] Benedikt Lassalle-Kaiser,[b,†] Andrea Zitolo,[b] Christel Laberty-Robert,[a] David Portehault[a,*]

[a] Sorbonne Université, CNRS, Laboratoire de Chimie de la Matière Condensée de Paris (CMCP), 4 place Jussieu, F-75005, Paris, France
[b] Synchrotron SOLEIL, L'Orme des Merisiers, Saint-Aubin, 91191 Gif-sur-Yvette, France
[c] Dpto. de Química Inorgánica I, Facultad de Ciencias Químicas, Universidad Complutense, 28040 Madrid, Spain

Corresponding author: david.portehault@sorbonne-universite.fr

† Current adress: ITODYS, CNRS, UMR086, Université Paris Cité, 15 rue Jean-Antoine de Baïf, 75013, Paris, France

Methods

Powder X-ray diffraction (XRD) diagrams were performed on a Bruker D8 Advance diffractometer operating at the Cu Kα wavelength (λ = 1.5418 Å). $Ni_2Si_{1-x}P_x$, *o*-Ni_2Si, $Ni_{31}Si_{12}$, Ni, Ni_2P, LiCl and KCl were identified according to the reference cards 04-005-5697 (PDF+4), 04-010-3516 (PDF+4), 111889 (ICDD), 00-004-0850 (PDF+4), 04-003-1863 (PDF+4), 00-004-0664 (PDF+4), and 00-041-1476, respectively.

X-ray photoelectron spectroscopy (XPS) analyses were performed on an Omicron Argus X-ray photoelectron spectrometer, equipped with a monochromated AlKα radiation source (1486.6 eV) and a 280 W electron beam power. Binding energies were calibrated against the C 1s (C-C) binding energy at 284.8 eV.

Transmission electron microscopy (TEM) images of Figures S1 and S2 were acquired on a Technai Spirit 2 microscope operating at 120 kV. **High-resolution transmission electron microscopy** (HRTEM) images of Figure 5 were obtained on a JEOL JEM 2100 FEG microscope (Tokyo, Japan) operating at 200 kV with a spatial punctual resolution of 1.8 Å equipped with X-ray Energy Dispersive Spectroscopy (EDS) for chemical analysis. A JEOL-JEM Grand ARM 300cF microscope (Madrid, Spain) equipped with a Cs Corrector (ETA-JEOL) and CMOS camera (4096 x 4096 pixels, Gatan OneView) at 120 kV was used for Figures 1B and D. Quantitative EDS was performed in TEM mode in a JEOL JEM 2100 microscope (Madrid, Spain) operating at 200 kV equipped an OXFORD INCA spectrometer. With the goal of achieving representative chemical information, 125 EDS spectra were acquired. The samples were prepared by drop-depositing ethanol or 1-butanol suspensions on carbon coated Cu grids in the air.

Scanning electron microscope-energy-dispersive X-ray spectroscopy (SEM-EDS) (Oxford Instruments – X-max) was performed on a scanning electron microscope HITACHI S3400N at 20 kV. Cobalt was used for calibration of quantitative analyses. Powder samples were flatly smeared on a carbon adhesive tape on sample holder. Spectra were recorded on three different zones for each sample.

Energy Electron Loss Spectroscopy (EELS) study was carried out in JEOL JSM-ARM200F (Madrid, Spain), cold emission gun, probe spherical aberration corrected microscope operating at 120 kV. Chemical distribution study was performed by using a GIF-QuantumER with a collection convergence semiangle of 18 mrad and 20.3 mrad, respectively. Spectrums were acquired by using spectrum line and 2D mode, with 0.25 eV dispersion and 0.05 s acquisition time and an over an average of 100 points per particle per line scan and 2000 per map. Principal component analysis (PCA) was performed on EELS data to improve signal to noise ratio by using the multivariate statistical analysis (MSA) plugins for GatanDMS software[1]. The sample was deposited by drop-casting on Cu-grids under air.

X-ray absorption near edge structure (XANES) data for Si K- and P K-edges were collected on the LUCIA beamline of synchrotron SOLEIL with a ring energy of 2.75 GeV. The incident beam energy was monochromatized using a Si (111) double crystal monochromator. Data were collected in a primary vacuum chamber as fluorescence spectra with an outgoing angle of 5° using a Bruker silicon drift detector. The data were normalized by the intensity of incident energy and processed with the Athena software. Powder samples were measured as ingots prepared by pressing mixtures of nanoparticles and boron nitride powders. Electrode samples were measured as prepared and as recovered for electrochemical measurement.

Ni K-edge X-ray absorption spectroscopy (XAS) for the Ni K-edge was conducted at room temperature at the SAMBA beamline of synchrotron SOLEIL. The beamline is equipped with a sagittally focusing Si 220 monochromator and two Pd-coated mirrors that were used to remove X-rays harmonics. For *ex situ* measurements, the catalysts were pelletized as disks of 10 mm diameter with 1 mm thickness using 2 mg sample powder and 40 mg cellulose powder as a binder. *In situ* measurements were performed by recording the K_α X-ray fluorescence of Ni with a Canberra 35-elements monolithic planar Ge pixel array detector with the catalyst deposited by drop-casting on the 100 µm-thick carbon substrate. The catalyst layer was probed through the carbon substrate in fluorescence mode by using a custom-made cell (**Figure below**).

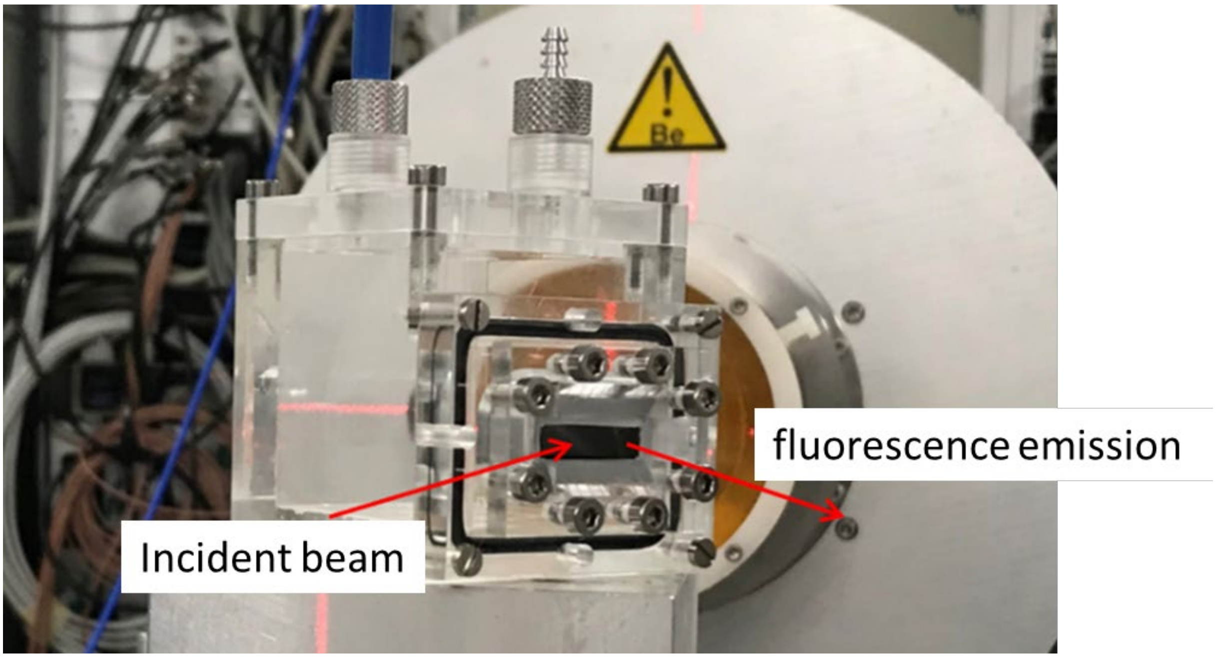

Custom-made electrochemical cell of three-electrode configuration for in situ XAS analysis.

***In situ* X-ray diffraction.** *In situ* X-ray diffraction experiments were carried out at the French SOLEIL Synchrotron facility on the DIFFABS beamline, in transmission mode at an energy (wavelength) of 17.878 keV (0.6935 Å). A double crystal monochromator equipped with two Si(1,1,1) crystals was used to tune the energy. We used a custom-made capillary oven described previously.[2] In brief, it enables performing X-ray diffraction *in situ* during controlled heating of the reaction mixture in a 1 mm-diameter quartz capillary opened under argon flow, to mimic the conditions of *ex situ* lab synthesis. For these experiments, we used a circular 2D detector covering 140° detection angle on only one acquisition.[3] The capillary was continuously scanned by sequentially monitoring 3 positions to probe the homogeneity of the medium. A diffractogram was acquired every 9 s, which corresponds to one diffractogram every 37 s for each position.

Working electrode preparation. Two types of working electrode substrates were used for different measurements. A glassy carbon (GC) rotating disk electrode (RDE) with a diameter of 5 mm was used for cyclic voltammetry (CV) and electrochemical impedance spectroscopy (EIS). A GC sheet was used for chronopotentiometry (CP) measurements and EIS before and after CP. The catalyst film was prepared by drop-casting. 3.5 mg of catalyst was sonicated in 480 µL absolute ethanol for 60 min, followed by addition of 20 µL of Nafion solution (5 % in alcohols and water, Sigma-Aldrich) for another 15 min of ultrasonication. The well-dispersed ink was then dropped onto the as-polished RDE or the GC sheet substrate to obtain a catalyst loading of 350 $\mu g_{catalyst} \cdot cm^{-2}_{electrode}$, and then the coating was dried under air for 30 min.

Measurements of OER properties. Electrochemical measurements were performed with a typical three-electrode configuration which includes the working electrode, a Pt coil as counter electrode and an Ag/AgCl in saturated KCl electrode as reference electrode. 0.1 M KOH was used as electrolyte (pH = 13). In order to remove the Fe impurity in the electrolyte, *ca*. 1 g of as-prepared $Ni(OH)_2$ solid was put into 200 mL as-prepared 0.1M KOH.[58] The suspension was sonicated for 3 min and then rested for at least 6 h. The purified 0.1M KOH supernatant was separated by centrifugation, stored under nitrogen and later used as electrolyte. Before measurements, the electrolyte was bubbled with O_2 for 20 min. The rotating disk electrode rotated at 1600 rpm. Cyclic voltammograms were recorded in the potential range of 0 to 1.05 V vs. Ag/AgCl reference electrode at a scan rate of 20 mV s^{-1}. For the chronopotentiometry measurement, a carbon sheet was used for working electrode substrate, a Teflon-coated stir bar was put in the electrolyte and stirred at 400 rpm to enhance the ions diffusion. For the potentials reported in this work, the ohmic drop iR was corrected by considering the total impedance measured at a frequency of 50 kHz as the solution resistance. The measured potentials were converted by the equation: $E_{RHE} = E_{measured} + 0.197 + 0.0591\times$ pH, where pH = 13. EIS spectra were fitted along the following equivalent electrical circuit whose components are described in the main text:

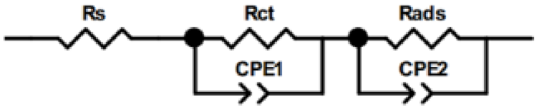

The spectra were fitted to an equivalent circuit (**Figure 4B** and experimental details in SI) with three components accounting for the solution resistance (R_s), the charge transfer resistance (R_{ct}) within the electrode, and the adsorption resistance (R_{ads}) related to the adsorption of reaction intermediates.[4,5]

Measurements of HER properties. The same configuration as for OER studies was used except that a carbon rod was used as counter electrode. 0.1 M KOH was used as electrolyte (pH = 13). Before measurements, the electrolyte was saturated by Ar bubbling for 20 min. The rotating disk electrode rotated at 1600 rpm. The potential was cycled in the range of -0.5 to -2.0 V vs. Ag/AgCl reference electrode at a scan rate of 20 mV s^{-1}. The parameters for OER CP measurement were followed for HER CP measurement.

***In situ* XAS experiments.** *In situ* XAS at the Ni-K edge was performed at the SAMBA beamline of SOLEIL synchrotron. The spectra were acquired by recording the K_α X-ray fluorescence of Ni with a Canberra 35-elements monolithic planar Ge pixel array detector. The electrochemical methods were the same as described above, except that the working electrode was installed in a different custom-made electrochemical cell of three-electrode configuration where one of the faces of the working electrode is exposed for X-ray analysis (**Figure S14**). Four electrochemical steps were used, including successively a first OCV measurement (~0.8 V vs. RHE) for 20 min during which an X-ray absorption spectrum was acquired, activation by cyclic voltammetry from 1.0 to 2.0 V vs. RHE for OER (from 0.5 to -1.0 V vs. RHE for HER), chronoamperometry (CA) for 25 min at 2.0 V vs. RHE for OER (at -0.5 V vs. RHE for HER) with simultaneous XAS measurement, and then a second OCV measurement with XAS acquisition. The ohmic drop iR correction was not carried out in these measurements. Meanwhile, the XAS spectra were acquired at four different states of the electrode. Firstly, the installed dry electrode was measured before adding electrolyte in the cell. Then, the electrode in contact with electrolyte was measured during the first OCV. A third measurement was performed during CA. Finally, the Ni K-edge XANES of the electrode was measured when it was brought back to the OCV. The acquisition of one spectrum took approx. 20 min to reach a satisfying signal-noise-ratio. XAS data processing were carried out on Athena© software.

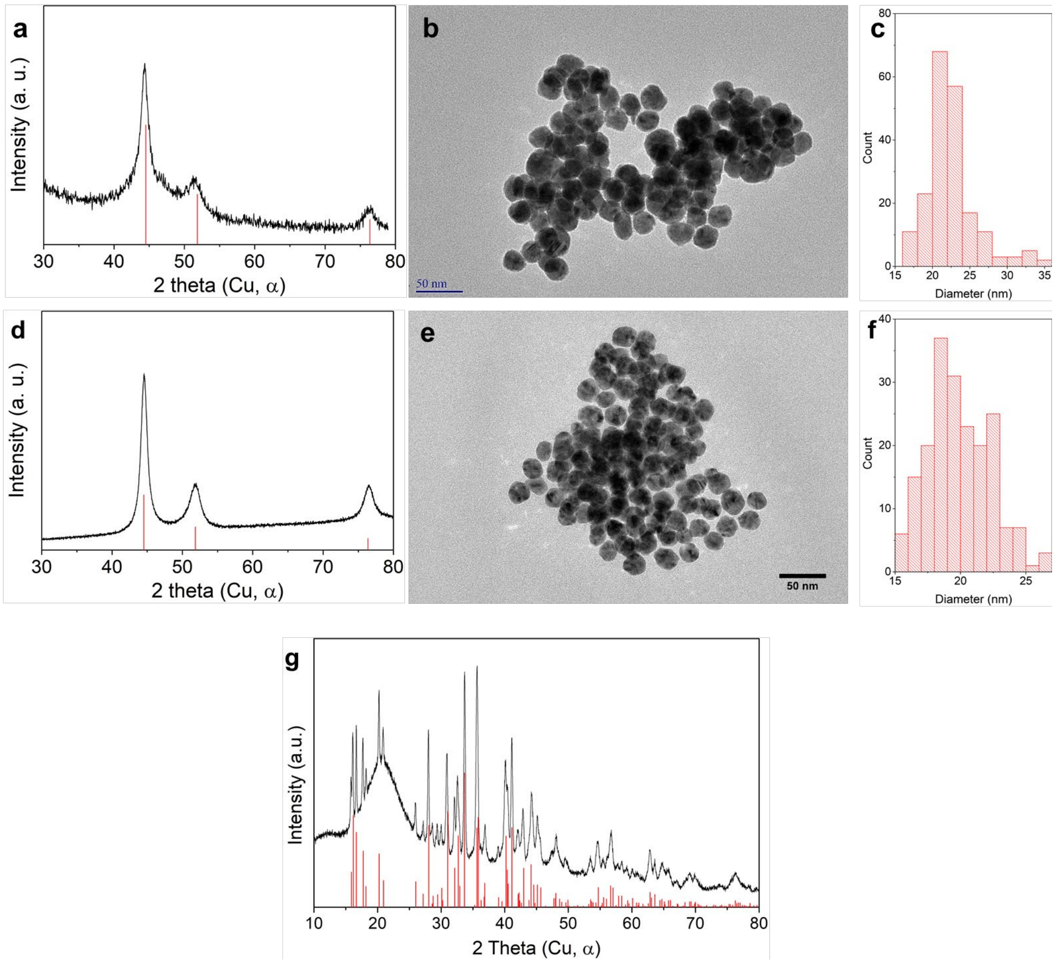

Figure S1. (a-c) TOP-capped Ni nanoparticles used as reagents for ternary nickel silicophosphide synthesis: (a) powder XRD pattern, red drop lines indicating Ni reference pattern; (b) TEM image and (c) corresponding size distribution. (d-f) Ni nanoparticles used as reagents for Ni_2Si synthesis: (d) powder XRD pattern, red drop lines indicating Ni reference, (e) TEM image and (f) size distribution. (g) Powder XRD pattern of as-prepared Na_4Si_4 used as reagent. Red drop lines indicate Na_4Si_4 reference pattern.

Table S1. Ni, Si and P ratio determined by SEM-EDS of Ni nanoparticle precursors and of their corresponding products. (*Determined by TEM-EDS). SEM-EDS indicates for $Ni_2Si_{1-x}P_x$ overall atomic ratios Ni:Si:P of 2:1.1:0.3, hence an excess of *p*-block elements compared to the composition of the particles according to TEM and Rietveld. This can be ascribed to *o*-Ni_2Si and Si impurities detected by XRD.

	Ni	Si	P
Ni nanoparticles (high P content)	2	/	0.3
$Ni_2Si_{1-x}P_x$	2	1.1	0.3
	2.0^*	0.9^*	0.4^*
Ni nanoparticles (low P content)	2	/	0.1
Ni_2Si	2	1.3	0.1

Table S2. Details of Rietveld refinement of the powder XRD pattern of $Ni_2Si_{0.7}P_{0.3}$ nanocrystals

Phase	$Ni_2Si_{0.7}P_{0.3}$	Ni_2Si	Si
Space group	$P\bar{6}2m$	$Pnma$	$Fd\bar{3}m$
a (Å)	6.0807(5)	4.965(3)	5.436(5)
b (Å)	6.0807(5)	3.8395(17)	5.436(5)
c (Å)	3.16159(17)	7.112(4)	5.436(5)
α, β (°)	90, 90	90, 90	90, 90
γ (°)	120	90	90
Volume (Å^3)	101.236(2)	135.579(6)	160.627(7)
Crystallite size (nm)	37	23	141
Weight fraction	0.898(3)	0.095(3)	0.0073(11)
R_{wp} (%)		4.31	

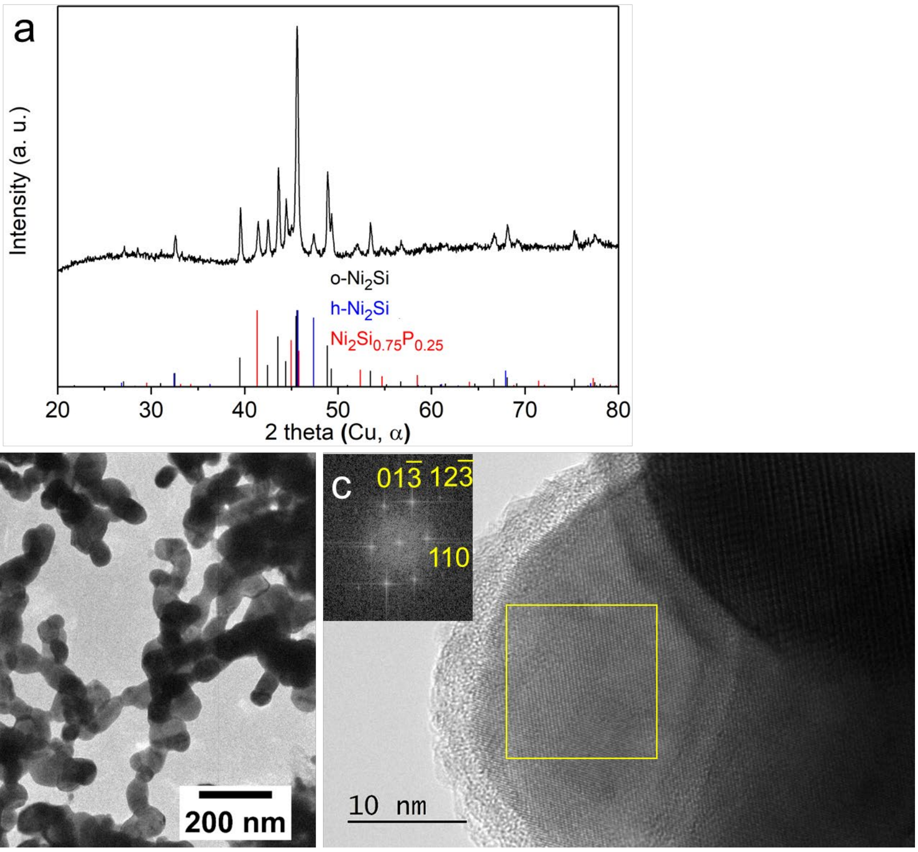

Figure S2. *o*-Ni_2Si nanoparticles obtained by conversion of Ni nanoparticles with low P content. (a) powder XRD pattern of the *o*-Ni_2Si product (reference patterns of *h*-N_2Si and $Ni_2Si_{0.75}P_{0.25}$ are displayed for comparison). (b) TEM image and (c) HRTEM and FFT of the yellow squared area. The FFT is fully indexed along the *o*-Ni_2Si structure.

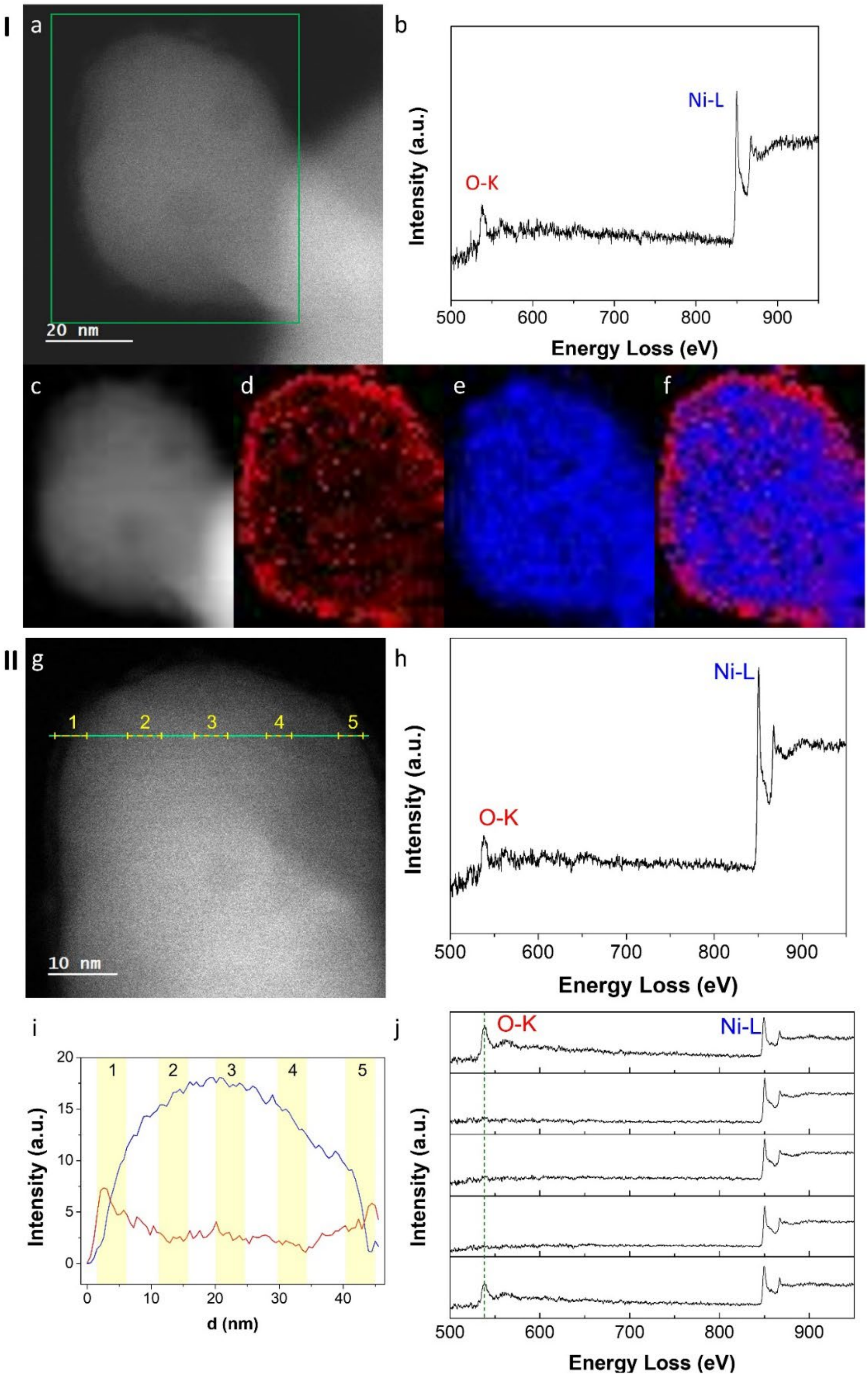

Figure S3. Chemical distribution in $Ni_{2.0}Si_{0.7}P_{0.3}$ nanoparticles studied by EEL spectroscopy by (I) 2D maps and (II) line profile analysis. (a, g) STEM-HAADF image and (b, h) EELS sum spectra, where O-K and Ni-L edges are displayed. Panel I: (c) STEM-HAADF image acquired simultaneously with the EELS maps, (d) O-K and (e) Ni-L chemical maps on the green area in (a) and (f) combined O and Ni maps. Panel II: (i) O and Ni EELS edges intensity profile and (j) sum spectrum trend at different positions along green line in (g).

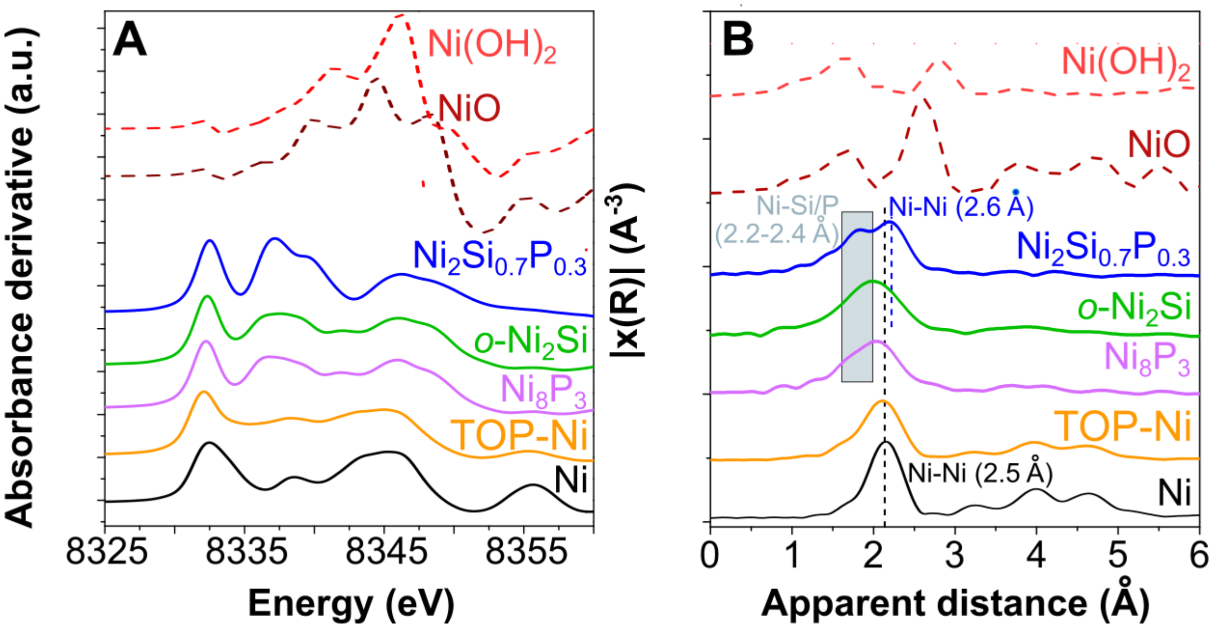

Figure S4. (A) First derivative of the XANES spectra shown in Figure 2A of the main text, where the first maxima are used to evaluate the Ni K-edge energy. (B) Fourier transform of the EXAFS spectra for the nickel silicophosphide and some references (not corrected for phase shift).

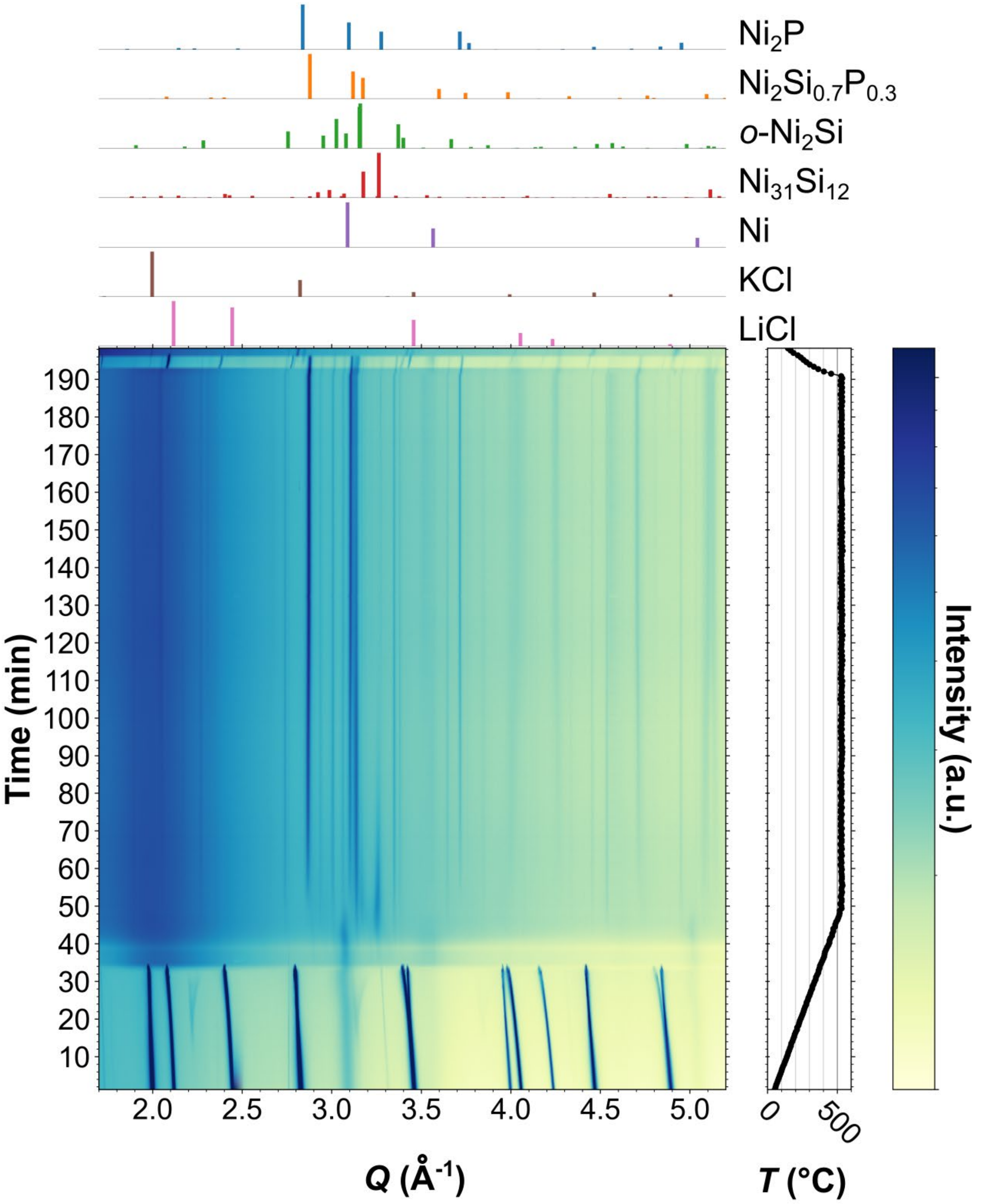

Figure S5. *In situ* XRD patterns recorded during heating of the reaction mixture at one position in the reaction capillary, analyzed in detail in **Figure 3**. The reflections of LiCl and KCl disappear at a measured temperature of 380 °C, which serves as an internal calibration point, thus corresponding to the tabulated melting temperature of 353 C. This ~30 °C discrepancy has been considered to fix the experimental plateau at a measured temperature of 530 °C, corresponding to actual 500 °C, which coincides with the temperature of lab synthesis. Accordingly, the temperatures discussed in the main text are corrected by -30 °C compared to the measured values displayed on Figures 3, S5-S8.

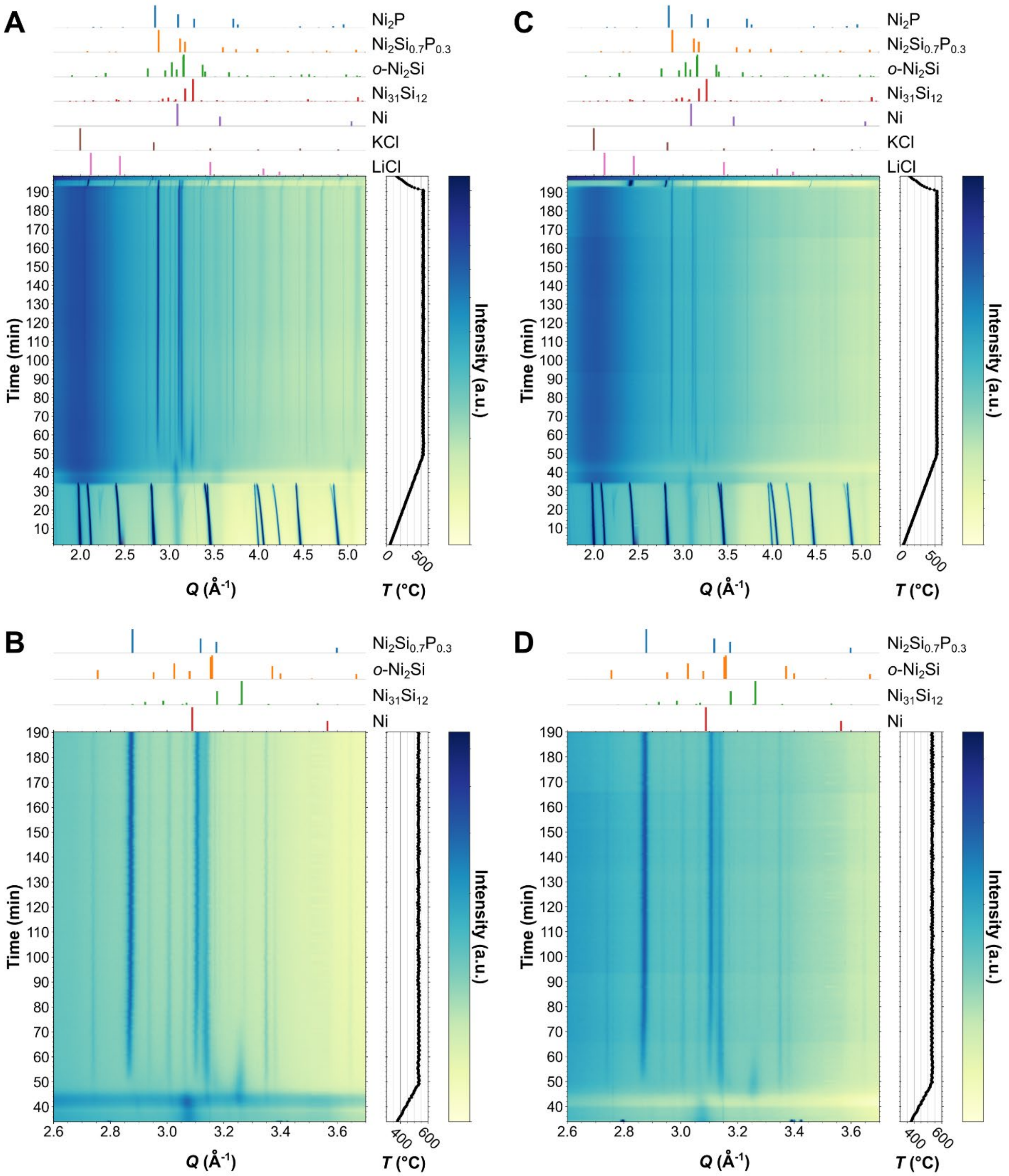

Figure S6. *In situ* XRD diagrams recorded during heating of the reaction mixture on two different positions in a capillary, which also differ from the position analyzed in **Figures S5** and **Figure 3** (all positions are separated by ca. 1 mm along the capillary): whole experiments are shown at the top, the corresponding zooms in the molten area are shown at the bottom. These positions in addition to the one used for Figures 3 and S5 exhibit very similar behaviors and show the homogeneity of the reaction mixture.

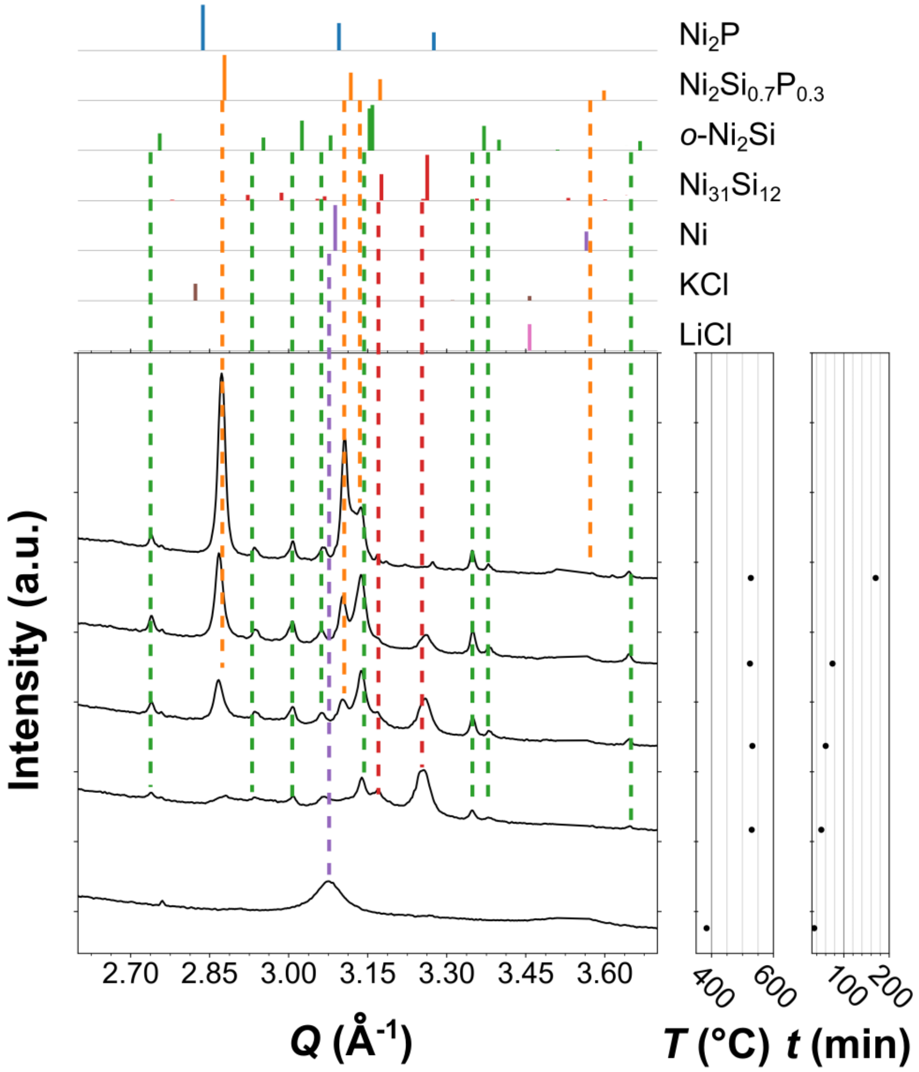

Figure S7. Selected *In situ* XRD patterns selected from the different areas in **Figure 3** after melting, and corresponding reference patterns. Note the absence of Ni_2P, and the shift of diffraction peaks to low *Q* values compared to references due to thermal expansion.

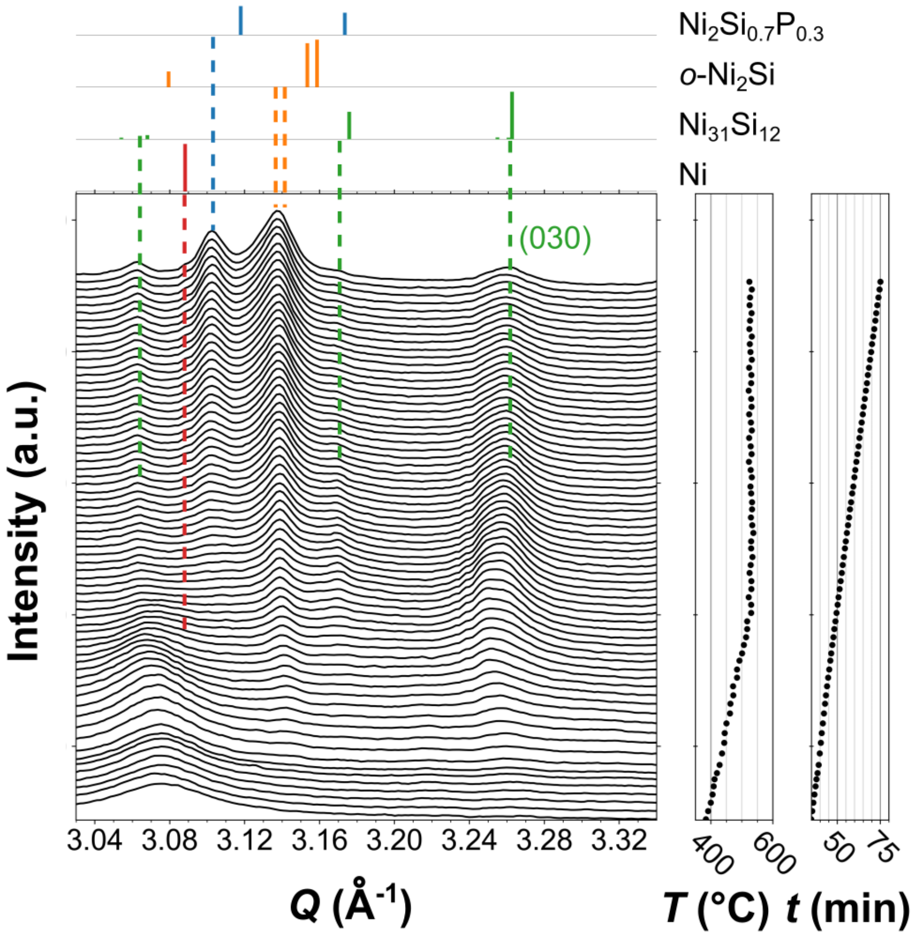

Figure S8. *In situ* XRD diagrams recorded during heating of the reaction mixture at the same capillary position as **Figures 3** and **S5**, showing the transformation from Ni to $Ni_{31}Si_{12}$ and the evolution of the $Ni_{31}Si_{12}$ main reflection (030) at *ca.* 3.26 Å. The corresponding temperatures and reaction times are plotted in front of each diagram on the two graphs on the left. Note that contrary to all other phases that show a shift of reflections to low *Q* values due to thermal expansion, the $Ni_{31}Si_{12}$ peak shifts to higher *Q* values upon heating.

Table S3. Comparison of charge transfer resistance R_{ct} and adsorption resistance R_{ads} derived from EIS for $Ni_2Si_{0.7}P_{0.3}$ and *o*-Ni_2Si electrodes at before and after 25 CV cycles under OER conditions.

Electrode	$Ni_2Si_{0.7}P_{0.3}$		*o*-Ni_2Si	
	Before CVs	After CVs	Before CVs	After CVs
R_{ct} (Ω)	5.2	5.8	9.3	9.6
R_{ads} (Ω)	4.5	3.8	27.0	5.5

Supplementary text: Identification of electrocatalytic species and elemental segregation during electrocatalysis.

***In situ* study of electrocatalysis.** *In situ* XANES at the Ni K-edge (**Figure 5**) shows that $Ni_2Si_{0.7}P_{0.3}$ is stable upon preparation of the electrode. In the oxygen-saturated electrolyte for OER (**Figures 5A, C** and **S9-Left**), the material is slightly oxidized upon immersion, then the contribution of oxidic species grows under OER conditions (2.0 V vs. RHE, **Figure 5C**), confirming that the OER activity arises from a nickel (oxyhydr)oxide layer. In the argon-saturated electrolyte for HER (**Figures 5B, D** and **S9-Right**), no significant change of the Ni K-edge occurs upon activation and HER operation (**Figure 5D**). *o*-Ni_2Si nanocrystals exhibit stronger structural reorganization (**Figure S10**), confirming that the silicide is less stable than the silicophosphide versus corrosion in alkaline conditions.

***Post catalysis* analyses.** The Si and P K-edges XANES (**Figure S11**) do not change significantly from the pristine $Ni_2Si_{0.7}P_{0.3}$ powder to the electrodes recovered after OER and HER. TEM (**Figure 6A, B**) shows an amorphous oxide layer on the nanocrystal surface (**Figure 6C, D**) that is thicker than on pristine nanocrystals (**Figure 1A**). The crystalline Ni_2P-like structure is maintained (**Figure 6C, D**), with Ni, Si and P remaining in the core according to STEM-HAADF and STEM-EDS (**Figure 6E, F**). SEM-EDS (**Table S4**) shows significant leaching of Si, while the P content evolves to a lower extent. This confirms that phosphorus enhances resistance to corrosion for alkaline water electrolysis. The oxidic layer from the reductive conditions of HER is surprising, but it may form during the recovery of the electrode after HER at the OCV and also during drying and air exposure. P could not be detected by XPS after OER and HER (**Figure S12**), which shows only oxidic Ni and Si species. Hence, the layer observed by TEM contains only oxidized Ni and Si and is too thick to enable XPS detection of phosphorus remaining in the silicophosphide core. The silicophosphide nanocrystals mostly retain their structure during electrocatalysis and are more resistant than the parent silicide versus corrosion in alkaline medium. A disordered (oxyhydr)oxide layer forms at the surface of the nanoparticles during electrocatalysis, especially in OER conditions, as with previously reported silicides and borosilicides,[2,6] but the silicophosphide exhibits a specific behavior, because the partitioning of the different *p*-block elements between the metallic core and the oxidic surface layer is differentiated.

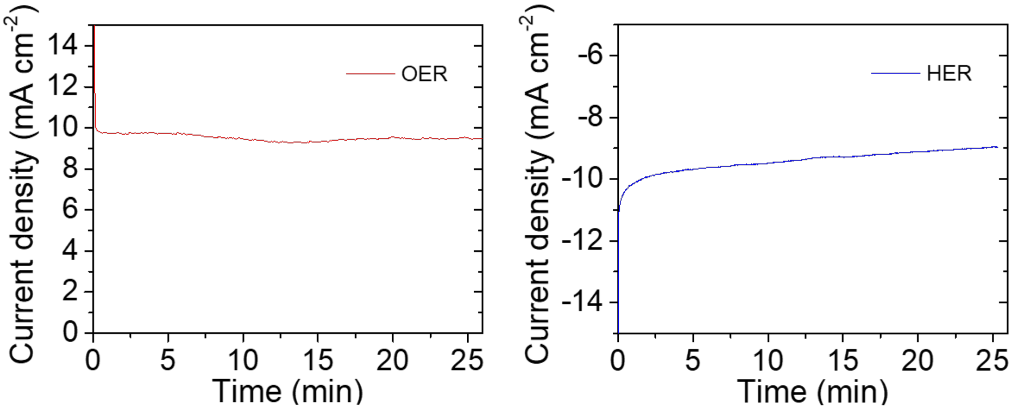

Figure S9. Chronoamperometry measurement during *in situ* XAS of $Ni_2Si_{0.7}P_{0.3}$ nanoparticles in an aqueous Fe-free O_2-saturated 0.1 M KOH electrolyte at 2.0 V vs. RHE for OER and -0.5 V vs. RHE for HER.

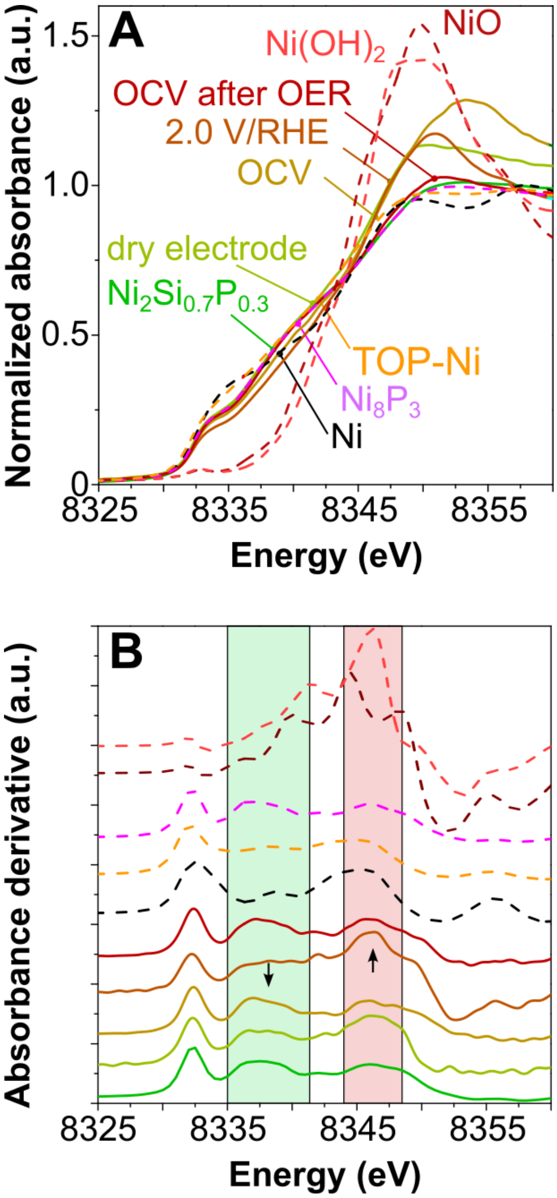

Figure S10. (A) *in situ* XANES spectra at Ni K-edge recorded on a o-Ni_2Si electrode at different stages of OER and (B) corresponding first derivatives: dry electrode before use, then *in situ* XANES at the open circuit voltage (OCV) and during chronoamperometry at 2.0 V vs. RHE for OER. Reference spectra of the initial *o*-Ni_2Si powder, a Ni foil, P-doped nickel nanoparticles, Ni_8P_3, NiO and $Ni(OH)_2$ are also shown for comparison. In B, the black arrows show a significant decrease (increase) of the silicide (NiO/$Ni(OH)_2$) component upon OER chronoamperometry, indicating large oxidation of *o*-Ni_2Si during OER operation, contrary to $Ni_2Si_{0.7}P_{0.3}$ (Figures 5 and S9), for which changes are much weaker.

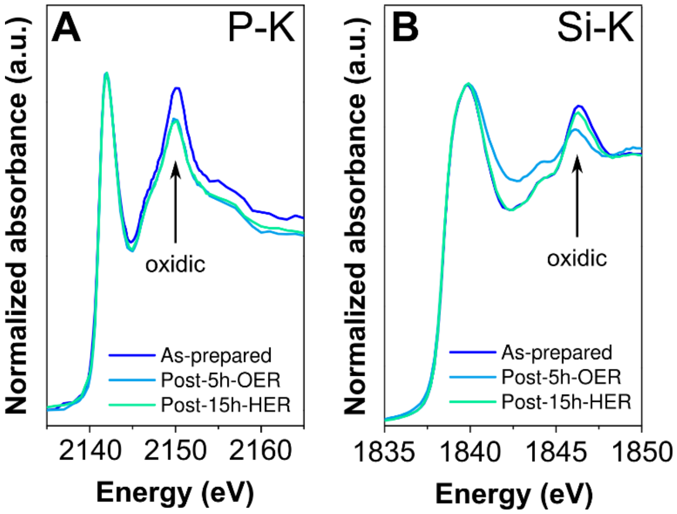

Figure S11. (A) P K- and (B) Si K-edges XANES recorded on $Ni_2Si_{0.7}P_{0.3}$ electrodes as-obtained, after OER and after HER.

Table S4. Ni, Si and P atomic contents before and after OER electrochemical measurement, measured on a $Ni_2Si_{0.7}P_{0.3}$ electrode by SEM-EDS.

	Ni	Si	P
t=0	2	1.1	0.3
Post-5h-OER	2	0.8	0.3

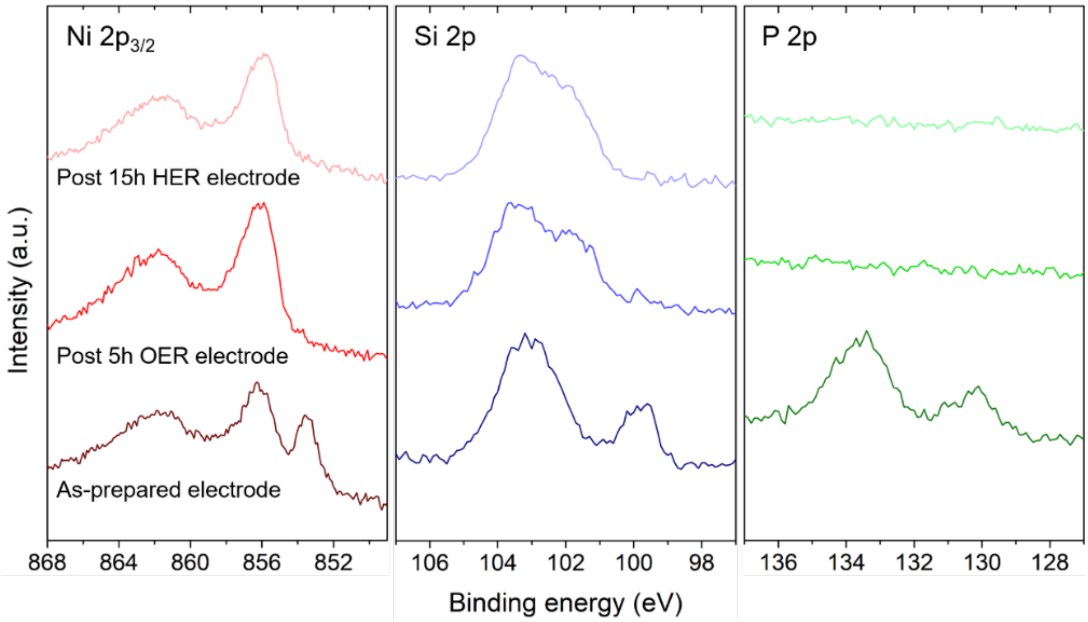

Figure S12. XPS of a $Ni_2Si_{0.7}P_{0.3}$ electrode before use, after 5h of OER and after 15h of HER electrode in the Ni 2p$_{3/2}$, Si 2p and P 2p regions. After catalysis, Ni and Si are detected only as oxidized species with peaks at binding energies of *ca.* 856 and 103 eV, respectively.

Supplementary references

1. Lucas, G., Burdet, P., Cantoni, M. & Hébert, C. Multivariate statistical analysis as a tool for the segmentation of 3D spectral data. *Micron* **52–53**, 49–56 (2013).
2. Janisch, D. *et al.* Covalent Transition Metal Borosilicides: Reaction Pathways in Molten Salts for Water Oxidation Electrocatalysis. *J. Am. Chem. Soc.* **146**, 21824–21836 (2024).
3. Desjardins, K. *et al.* The CirPAD, a circular 1.4 M hybrid pixel detector dedicated to X-ray diffraction measurements at Synchrotron SOLEIL. *J. Synchrotron Radiat.* **29**, 180–193 (2022).
4. Franco, D. V., Silva, L. M. D., Jardim, W. F. & Boodts, J. F. C. Influence of the electrolyte composition on the kinetics of the oxygen evolution reaction and ozone production processes. *J. Braz. Chem. Soc.* **17**, 446–757 (2006).
5. Qi, J. *et al.* Porous Nickel–Iron Oxide as a Highly Efficient Electrocatalyst for Oxygen Evolution Reaction. *Adv. Sci.* **2**, 1500199 (2015).
6. Song, Y. *et al.* Heterostructured Cobalt Silicide Nanocrystals: Synthesis in Molten Salts, Ferromagnetism, and Electrocatalysis. *J. Am. Chem. Soc.* **145**, 19207–19217 (2023).